

Colliders and Cosmology

Keith A. Olive^a

William I. Fine Theoretical Physics Institute, University of Minnesota, Minneapolis, MN 55455, USA

Received: date / Revised version: date

Abstract. Dark matter in variations of constrained minimal supersymmetric standard models will be discussed. Particular attention will be given to the comparison between accelerator and direct detection constraints.

PACS. PACS-key describing text of that key – PACS-key describing text of that key

1 Introduction

Evidence for dark matter in the universe is available from a wide range of observational data. In addition to the classic evidence from galactic rotation curves [1], the analysis of the cosmic microwave background anisotropies leads to the conclusion that the curvature of the universe is close to zero indicating that the sum of the fractions of critical density, Ω , in matter and a cosmological constant (or dark energy) is close to one [2]. When combined with a variety of data including results from the analysis of type Ia supernovae observations [3] and baryon acoustic oscillations [4] one is led to the concordance model where $\Omega_m \sim 0.23$ and $\Omega_\Lambda \sim 0.73$ with the remainder (leading to $\Omega_{tot} = 1$) in baryonic matter. Other dramatic pieces of evidence can be found in combinations of X-ray observations and weak lensing showing the superposition of dark matter (from lensing) and ordinary matter from X-ray gas [5] and from the separation of baryonic and dark matter after the collision of two galaxies as seen in the Bullet cluster [6]. For a more complete discussion see [7].

Here, I will adopt the results of the three-year data from WMAP [2] which has determined many cosmological parameters to unprecedented precision. Of particular interest is the determination of the total matter density (relative to the critical density), $\Omega_m h^2$ and the baryonic density, $\Omega_b h^2$. In the context of the Λ CDM model, the WMAP only results indicate

$$\Omega_m h^2 = 0.1265_{-0.0080}^{+0.0081} \quad \Omega_b h^2 = 0.0223 \pm 0.0007 \quad (1)$$

The difference corresponds to the requisite dark matter density

$$\Omega_{CDM} h^2 = 0.1042_{-0.0080}^{+0.0081} \quad (2)$$

or a 2σ range of $0.0882 - 0.1204$ for $\Omega_{CDM} h^2$.

^a To be published in “Supersymmetry on the Eve of the LHC” a special volume of European Physical Journal C, Particles and Fields (EPJC) in memory of Julius Wess.

2 Constrained MSSM models

To construct the supersymmetric standard model [8] we start with the complete set of chiral fermions needed in the standard model, and add a scalar superpartner to each Weyl fermion so that each field in the standard model corresponds to a chiral multiplet. Similarly we must add a gaugino for each of the gauge bosons in the standard model making up the gauge multiplets. The minimal supersymmetric standard model (MSSM) [9] is defined by its minimal field content (which accounts for the known standard model fields) and minimal superpotential necessary to account for the known Yukawa mass terms. As such we define the MSSM by the superpotential

$$W = \epsilon_{ij} [y_e H_1^j L^i e^c + y_d H_1^j Q^i d^c + y_u H_2^i Q^j u^c] + W_\mu \quad (3)$$

where

$$W_\mu = \epsilon_{ij} \mu H_1^i H_2^j \quad (4)$$

In (3), the indices, $\{ij\}$, are $SU(2)_L$ doublet indices. The Yukawa couplings, y , are all 3×3 matrices in generation space. Note that there is no generation index for the Higgs multiplets. Color and generation indices have been suppressed in the above expression. There are two Higgs doublets in the MSSM. This is a necessary addition to the standard model which can be seen as arising from the holomorphic property of the superpotential. That is, there would be no way to account for all of the Yukawa terms for both up-type and down-type multiplets with a single Higgs doublet. To avoid a massless Higgs state, a mixing term W_μ must be added to the superpotential.

In order to preserve the hierarchy between the electroweak and GUT or Planck scales, it is necessary that the explicit breaking of supersymmetry be done softly, i.e., by the insertion of weak scale mass terms in the Lagrangian. This ensures that the theory remain free of quadratic divergences [10]. The possible forms for such terms are

$$\mathcal{L}_{soft} = -\frac{1}{2} M_\lambda^a \lambda^a \lambda^a - \frac{1}{2} (m^2)_j^i \phi_i \phi_j^*$$

$$-\frac{1}{2}(BM)^{ij}\phi_i\phi_j - \frac{1}{6}(Ay)^{ijk}\phi_i\phi_j\phi_k + h.c. \quad (5)$$

where the M_λ^a are gaugino masses, m^2 are soft scalar masses, B is a bilinear mass term, and A is a trilinear mass term. Masses for the gauge bosons are of course forbidden by gauge invariance and masses for chiral fermions are redundant as such terms are explicitly present in M^{ij} already. For a more complete discussion of supersymmetry and the construction of the MSSM see [11].

2.1 Neutralinos and the Relic Density

There are four neutralinos, each of which is a linear combination of the $R = -1$ neutral fermions[12]: the wino \tilde{W}^3 , the partner of the 3rd component of the $SU(2)_L$ gauge boson; the bino, \tilde{B} ; and the two neutral Higgsinos, \tilde{H}_1 and \tilde{H}_2 . The mass and composition of the LSP are determined by the gaugino masses, μ , and $\tan\beta$. In general, neutralinos can be expressed as a linear combination

$$\chi = \alpha\tilde{B} + \beta\tilde{W}^3 + \gamma\tilde{H}_1 + \delta\tilde{H}_2 \quad (6)$$

The solution for the coefficients α, β, γ and δ for neutralinos that make up the LSP can be found by diagonalizing the mass matrix

$$(\tilde{W}^3, \tilde{B}, \tilde{H}_1^0, \tilde{H}_2^0) \begin{pmatrix} M_2 & 0 & \frac{-g_2 v_1}{\sqrt{2}} & \frac{g_2 v_2}{\sqrt{2}} \\ 0 & M_1 & \frac{g_1 v_1}{\sqrt{2}} & \frac{-g_1 v_2}{\sqrt{2}} \\ \frac{-g_2 v_1}{\sqrt{2}} & \frac{g_1 v_1}{\sqrt{2}} & 0 & -\mu \\ \frac{g_2 v_2}{\sqrt{2}} & \frac{-g_1 v_2}{\sqrt{2}} & -\mu & 0 \end{pmatrix} \begin{pmatrix} \tilde{W}^3 \\ \tilde{B} \\ \tilde{H}_1^0 \\ \tilde{H}_2^0 \end{pmatrix} \quad (7)$$

where $M_1(M_2)$ is a soft supersymmetry breaking term giving mass to the $U(1)$ ($SU(2)$) gaugino(s).

The relic abundance of LSP's is determined by solving the Boltzmann equation for the LSP number density in an expanding Universe,

$$\frac{dn}{dt} = -3\frac{\dot{R}}{R}n - \langle\sigma v\rangle(n^2 - n_0^2) \quad (8)$$

where n_0 is the equilibrium number density of neutralinos. By defining the quantity $f = n/T^3$, we can rewrite this equation in terms of $x \equiv T/m_\chi$, as

$$\frac{df}{dx} = m_\chi \left(\frac{8\pi^3}{90} G_{NN} \right)^{1/2} (f^2 - f_0^2) \quad (9)$$

The solution to this equation at late times (small x) yields a constant value of f , so that $n \propto T^3$.

The technique[13] used to determine the relic density is similar to that for computing the relic abundance of massive neutrinos[14] with the appropriate substitution of the cross section. The relic density depends on additional parameters in the MSSM beyond M_1, M_2, μ , and $\tan\beta$. These include the sfermion masses, $m_{\tilde{f}}$ and the Higgs pseudo-scalar mass, m_A . To determine the relic density it is necessary to obtain the general annihilation cross-section for neutralinos. In much of the parameter space

of interest, the LSP is a bino and the annihilation proceeds mainly through sfermion exchange. Because of the p-wave suppression associated with Majorana fermions, the s-wave part of the annihilation cross-section is suppressed by the outgoing fermion masses. This means that it is necessary to expand the cross-section to include p-wave corrections which can be expressed as a term proportional to the temperature if neutralinos are in equilibrium. Unless the neutralino mass happens to lie near a pole, such as $m_\chi \simeq m_Z/2$ or $m_h/2$, in which case there are large contributions to the annihilation through direct s-channel resonance exchange, the dominant contribution to the $\tilde{B}\tilde{B}$ annihilation cross section comes from crossed t-channel sfermion exchange.

Annihilations in the early Universe continue until the annihilation rate $\Gamma \simeq \sigma v n_\chi$ drops below the expansion rate. The final neutralino relic density expressed as a fraction of the critical energy density can be written as[12]

$$\Omega_\chi h^2 \simeq 1.9 \times 10^{-11} \left(\frac{T_\chi}{T_\gamma} \right)^3 N_f^{1/2} \left(\frac{\text{GeV}}{ax_f + \frac{1}{2}bx_f^2} \right) \quad (10)$$

where $(T_\chi/T_\gamma)^3$ accounts for the subsequent reheating of the photon temperature with respect to χ , due to the annihilations of particles with mass $m < x_f m_\chi$ [15] and $x_f = T_f/m_\chi$ is proportional to the freeze-out temperature. The coefficients a and b are related to the partial wave expansion of the cross-section, $\sigma v = a + bx + \dots$. Eq. (10) results in a very good approximation to the relic density expect near s-channel annihilation poles, thresholds and in regions where the LSP is nearly degenerate with the next lightest supersymmetric particle[16].

When there are several particle species i , which are nearly degenerate in mass, co-annihilations are important. In this case[16], the rate equation (8) still applies, provided n is interpreted as the total number density,

$$n \equiv \sum_i n_i, \quad (11)$$

n_0 as the total equilibrium number density,

$$n_0 \equiv \sum_i n_{0,i}, \quad (12)$$

and the effective annihilation cross section as

$$\langle\sigma_{\text{eff}}v_{\text{rel}}\rangle \equiv \sum_{ij} \frac{n_{0,i}n_{0,j}}{n_0^2} \langle\sigma_{ij}v_{\text{rel}}\rangle. \quad (13)$$

In eq. (9), m_χ is now understood to be the mass of the lightest sparticle under consideration.

2.2 The CMSSM

In its generality, the minimal supersymmetric standard model (MSSM) has over 100 undetermined parameters. But in addition to relieving the helplessness of an analysis with so many free parameters, there are good arguments based on grand unification [17] and supergravity

[18] which lead to a strong reduction in the number of parameters. I will assume several unification conditions placed on the supersymmetric parameters. In all models considered, the gaugino masses are assumed to be unified at the GUT scale with value, $m_{1/2}$, as are the trilinear couplings with value A_0 . Also common to all models considered here is the unification of all soft scalar masses set equal to m_0 at the GUT scale. With this set of boundary conditions at the GUT scale, we can use the the radiative electroweak symmetry breaking conditions by specifying the ratio of the two Higgs vacuum expectation values, $\tan\beta$, and the mass, M_Z , to predict the values of the Higgs mixing mass parameter, μ and the bilinear coupling, B . The sign of μ remains free. This class of models is often referred to as the constrained MSSM (CMSSM) [19, 20, 21, 22, 23]. In the CMSSM, the solutions for μ generally lead to a lightest neutralino which is very nearly a pure \tilde{B} .

Having set the boundary conditions at the GUT scale, renormalization group equations are run down to the electroweak scale. For example, at 1-loop, the RGEs for the gaugino masses are:

$$\frac{dM_i}{dt} = -b_i\alpha_i M_i/4\pi \quad (14)$$

Assuming a common gaugino mass, $m_{1/2}$ at the GUT scale as was discussed earlier, these equations are easily solved in terms of the fine structure constants,

$$M_i(t) = \frac{\alpha_i(t)}{\alpha_i(M_{GUT})} m_{1/2} \quad (15)$$

This implies that

$$\frac{M_1}{g_1^2} = \frac{M_2}{g_2^2} = \frac{M_3}{g_3^2} \quad (16)$$

(Actually, in a GUT, one must modify the relation due to the difference between the U(1) factors in the GUT and the standard model, so that we have $M_1 = \frac{5}{3} \frac{\alpha_1}{\alpha_2} M_2$.) At two loops, these relations are modified.

In the figure below, an example of the running of the mass parameters in the CMSSM is shown. Here, we have chosen $m_{1/2} = 250$ GeV, $m_0 = 100$ GeV, $\tan\beta = 3$, $A_0 = 0$, and $\mu < 0$. Indeed, it is rather amazing that from so few input parameters, all of the masses of the supersymmetric particles can be determined. The characteristic features that one sees in the figure, are for example, that the colored sparticles are typically the heaviest in the spectrum. This is due to the large positive correction to the masses due to α_3 in the RGE's. Also, one finds that the \tilde{B} , is typically the lightest sparticle. But most importantly, notice that one of the Higgs mass², goes negative triggering electroweak symmetry breaking [24]. (The negative sign in the figure refers to the sign of the mass², even though it is the mass of the sparticles which is depicted.)

Although the CMSSM is often confused in name with mSUGRA, i.e. models based on minimal supergravity, [25, 18], the latter employ two additional constraints [26]. In the simplest version of the theory[27, 25, 18] where supersymmetry is broken in a hidden sector, the universal trilinear soft supersymmetry-breaking terms are $A_0 = (3 -$

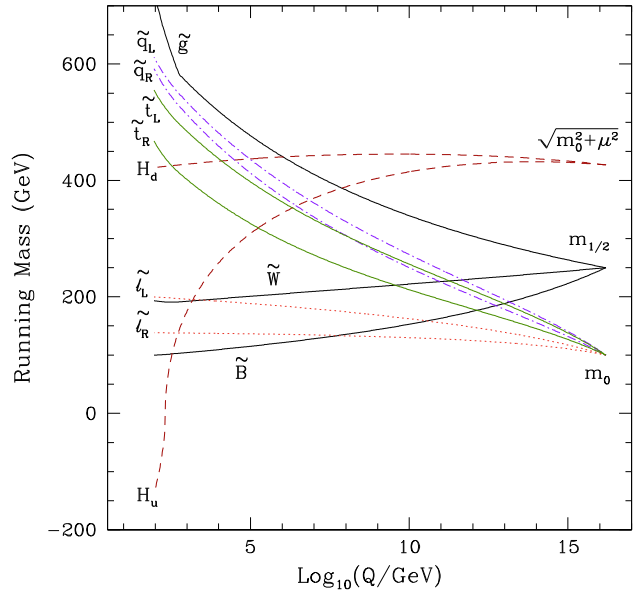


Fig. 1. RG evolution of the mass parameters in the CMSSM. I thank Toby Falk for providing this figure.

$\sqrt{3})m_0$ and bilinear soft supersymmetry-breaking term is $B_0 = (2 - \sqrt{3})m_0$, i.e., a special case of a general relation between B and A , $B_0 = A_0 - m_0$.

Given a relation between B_0 and A_0 , we can no longer use the standard CMSSM boundary conditions, in which $m_{1/2}$, m_0 , A_0 , $\tan\beta$, and $\text{sgn}(\mu)$ are input at the GUT scale with μ and B determined by the electroweak symmetry breaking condition. Now, one is forced to input B_0 and instead $\tan\beta$ is calculated from the minimization of the Higgs potential[26].

In addition, there is a relation between the gravitino mass and soft scalar masses, $m_{3/2} = m_0$. When electroweak symmetry breaking boundary conditions are applied, this theory contains only $m_{1/2}$, m_0 , and A_0 in addition to the sign of μ , as free parameters. The magnitude of μ as well as $\tan\beta$ are predicted.

In contrast to the mSUGRA model which contains one fewer parameter than the CMSSM, the remaining models to be discussed below are less constrained than the CMSSM, in that they involve more free parameters. One is a GUT-less model [28]. It is GUT-less in the sense that the supersymmetry breaking masses are unified not at the GUT scale, but at an input scale chosen to be below the GUT scale. This input parameter, M_{in} , is the one additional parameter relative to the CMSSM in the GUT-less models. Gauge coupling unification still occurs at the GUT scale. In the second class of models, the NUHM, the Higgs soft masses are not unified at the GUT scale [29, 30]. In this class of models, both μ and the Higgs pseudo scalar mass become free parameters.

In all of the models discussed below, I will assume unbroken $R - parity$ and hence the lightest supersym-

metric particle is stable. This will often, but not always be the neutralino [12].

3 The CMSSM after WMAP

For a given value of $\tan\beta$, A_0 , and $\text{sgn}(\mu)$, the resulting regions of acceptable relic density and which satisfy the phenomenological constraints can be displayed on the $m_{1/2} - m_0$ plane. In Fig. 2a, the light shaded region corresponds to that portion of the CMSSM plane with $\tan\beta = 10$, $A_0 = 0$, and $\mu > 0$ such that the computed relic density yields the WMAP value given in eq. (2) [22]. The bulk region at relatively low values of $m_{1/2}$ and m_0 , tapers off as $m_{1/2}$ is increased. At higher values of m_0 , annihilation cross sections are too small to maintain an acceptable relic density and $\Omega_\chi h^2$ is too large. Although sfermion masses are also enhanced at large $m_{1/2}$ (due to RGE running), co-annihilation processes between the LSP and the next lightest sparticle (in this case the $\tilde{\tau}$) enhance the annihilation cross section and reduce the relic density. This occurs when the LSP and NLSP are nearly degenerate in mass. The dark shaded region has $m_{\tilde{\tau}} < m_\chi$ and is excluded. The effect of coannihilations is to create an allowed band about 25-50 GeV wide in m_0 for $m_{1/2} \lesssim 950$ GeV, or $m_{1/2} \lesssim 400$ GeV, which tracks above the $m_{\tilde{\tau}_1} = m_\chi$ contour [31].

Also shown in Fig. 2a are the relevant phenomenological constraints. These include the LEP limits on the chargino mass: $m_{\chi^\pm} > 104$ GeV [32], on the selectron mass: $m_{\tilde{e}} > 99$ GeV [33] and on the Higgs mass: $m_h > 114$ GeV [34]. The former two constrain $m_{1/2}$ and m_0 directly via the sparticle masses, and the latter indirectly via the sensitivity of radiative corrections to the Higgs mass to the sparticle masses, principally $m_{\tilde{t},\tilde{b}}$. `FeynHiggs` [35] is used for the calculation of m_h . The Higgs limit imposes important constraints principally on $m_{1/2}$ particularly at low $\tan\beta$. Another constraint is the requirement that the branching ratio for $b \rightarrow s\gamma$ is consistent with the experimental measurements [36]. These measurements agree with the Standard Model, and therefore provide bounds on MSSM particles [37], such as the chargino and charged Higgs masses, in particular. Typically, the $b \rightarrow s\gamma$ constraint is more important for $\mu < 0$, but it is also relevant for $\mu > 0$, particularly when $\tan\beta$ is large. The constraint imposed by measurements of $b \rightarrow s\gamma$ also excludes small values of $m_{1/2}$. Finally, there are regions of the $(m_{1/2}, m_0)$ plane that are favoured by the BNL measurement [38] of $g_\mu - 2$ at the 2- σ level, corresponding to a deviation from the Standard Model calculation [39] using e^+e^- data.

Another mechanism for extending the allowed regions in the CMSSM to large m_χ is rapid annihilation via a direct-channel pole when $m_\chi \sim \frac{1}{2}m_A$ [19,21]. Since the heavy scalar and pseudoscalar Higgs masses decrease as $\tan\beta$ increases, eventually $2m_\chi \simeq m_A$ yielding a ‘funnel’ extending to large $m_{1/2}$ and m_0 at large $\tan\beta$, as seen in Fig. 2b. As one can see, the impact of the Higgs mass constraint is reduced (relative to the case with $\tan\beta = 10$) while that of $b \rightarrow s\gamma$ is enhanced.

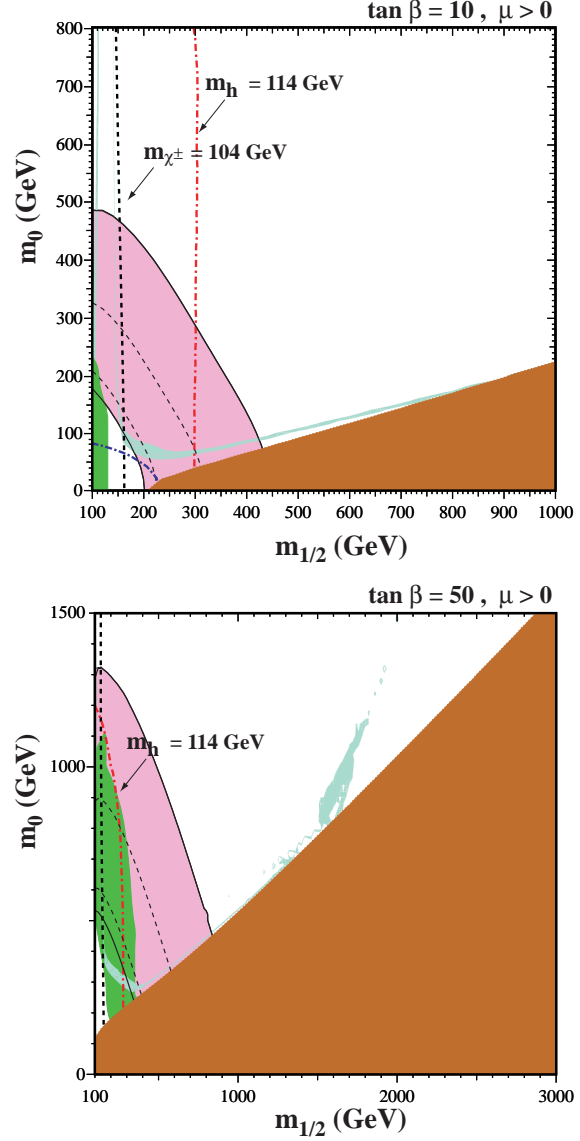


Fig. 2. The $(m_{1/2}, m_0)$ planes for (a) $\tan\beta = 10$ and $\mu > 0$, assuming $A_0 = 0$, $m_t = 175$ GeV and $m_b(m_b)_{SM}^{\overline{MS}} = 4.25$ GeV. The near-vertical (red) dot-dashed lines are the contours $m_h = 114$ GeV, and the near-vertical (black) dashed line is the contour $m_{\chi^\pm} = 104$ GeV. Also shown by the dot-dashed curve in the lower left is the corner excluded by the LEP bound of $m_{\tilde{e}} > 99$ GeV. The medium (dark green) shaded region is excluded by $b \rightarrow s\gamma$, and the light (turquoise) shaded area is the cosmologically preferred region. In the dark (brick red) shaded region, the LSP is the charged $\tilde{\tau}_1$. The region allowed by the E821 measurement of a_μ at the 2- σ level, is shaded (pink) and bounded by solid black lines, with dashed lines indicating the 1- σ ranges. In (b), $\tan\beta = 50$.

Shown in Fig. 3 are the WMAP lines [22] of the $(m_{1/2}, m_0)$ plane for $\mu > 0$ and values of $\tan\beta$ from 5 to 55, in steps $\Delta(\tan\beta) = 5$. We notice immediately that the strips are considerably narrower than the spacing between them, though any intermediate point in the $(m_{1/2}, m_0)$ plane would be compatible with some intermediate value of $\tan\beta$.

The right (left) ends of the strips correspond to the maximal (minimal) allowed values of $m_{1/2}$ and hence m_χ . The lower bounds on $m_{1/2}$ are due to the Higgs mass constraint for $\tan\beta \leq 23$, but are determined by the $b \rightarrow s\gamma$ constraint for higher values of $\tan\beta$.

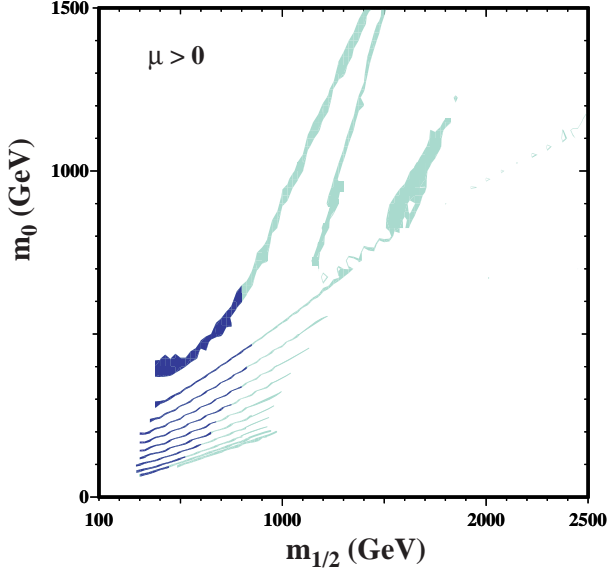


Fig. 3. The strips display the regions of the $(m_{1/2}, m_0)$ plane that are compatible with the WMAP determination of $\Omega_\chi h^2$ and the laboratory constraints for $\mu > 0$ and $\tan\beta = 5, 10, 15, 20, 25, 30, 35, 40, 45, 50, 55$. The parts of the strips compatible with $g_\mu - 2$ at the $2\text{-}\sigma$ level have darker shading.

Finally, there is one additional region of acceptable relic density known as the focus-point region [40], which is found at very high values of m_0 . An example showing this region is found in Fig. 4, plotted for $\tan\beta = 10$, $\mu > 0$, and $m_t = 175$ TeV. As m_0 is increased, the solution for μ at low energies as determined by the electroweak symmetry breaking conditions eventually begins to drop. When $\mu \lesssim m_{1/2}$, the composition of the LSP gains a strong Higgsino component and as such the relic density begins to drop precipitously. As m_0 is increased further, there are no longer any solutions for μ . This occurs in the shaded region in the upper left corner of Fig. 4. The position of the focus point strip is very sensitive to the value of m_t [41].

4 Direct detection

Direct detection techniques rely on the neutralino nucleon scattering cross-section. In general, there are two contributions to the low-energy effective four-fermion Lagrangian which are not velocity dependent. These can be expressed as spin-dependent and scalar or spin-independent interactions,

$$\mathcal{L} = \alpha_{2i} \bar{\chi} \gamma^\mu \gamma^5 \chi \bar{q}_i \gamma_\mu \gamma^5 q_i + \alpha_{3i} \bar{\chi} \chi \bar{q}_i q_i. \quad (17)$$

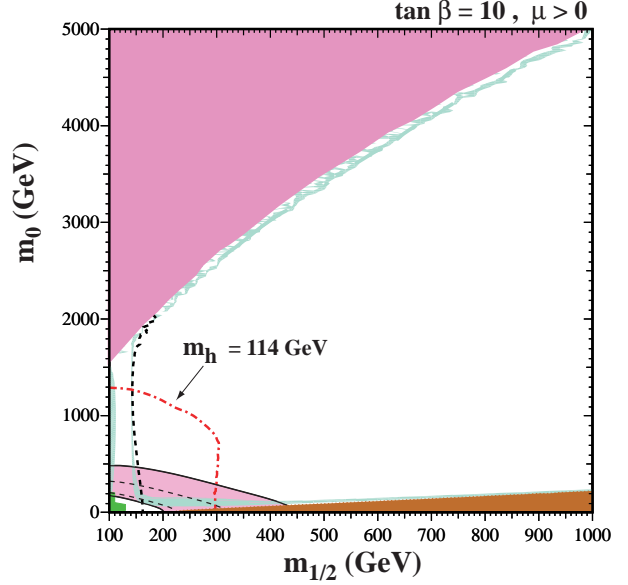


Fig. 4. As in Fig. 2a, where the range in m_0 is extended to 5 TeV. In the shaded region at very high m_0 , there are no solutions for μ which respect the low energy electroweak symmetry breaking conditions.

which is to be summed over the quark flavours q , and the subscript i labels up-type quarks ($i = 1$) and down-type quarks ($i = 2$). The detailed expressions for α_{2i} and α_{3i} can be found in [42].

The scalar cross section for a neutralino scattering on a nucleus with atomic number A and charge Z , can be written in terms of α_{3i} ,

$$\sigma_3 = \frac{4m_r^2}{\pi} [Zf_p + (A - Z)f_n]^2, \quad (18)$$

where m_r is the reduced LSP mass,

$$\frac{f_p}{m_p} = \sum_{q=u,d,s} f_{Tq}^{(p)} \frac{\alpha_{3q}}{m_q} + \frac{2}{27} f_{TG}^{(p)} \sum_{c,b,t} \frac{\alpha_{3q}}{m_q}, \quad (19)$$

the parameters $f_{Tq}^{(p)}$ are defined by

$$m_p f_{Tq}^{(p)} \equiv \langle p | m_q \bar{q} q | p \rangle \equiv m_q B_q, \quad (20)$$

$f_{TG}^{(p)} = 1 - \sum_{q=u,d,s} f_{Tq}^{(p)}$ [43], and f_n has a similar expression. The needed matrix elements are determined in part by the π -nucleon Σ term, which is given by

$$\sigma_{\pi N} \equiv \Sigma = \frac{1}{2} (m_u + m_d) (B_u + B_d). \quad (21)$$

and the strangeness contribution to the proton mass,

$$y = \frac{2B_s}{B_u + B_d} = 1 - \frac{\sigma_0}{\Sigma} \quad (22)$$

where σ_0 is the change in the nucleon mass due to the non-zero u, d quark masses, which is estimated on the basis of

Table 1. Matrix elements in terms of proton strangeness

Σ (MeV)	y	f_{T_u}	f_{T_d}	f_{T_s}
45	0.2	0.020	0.026	0.117
64	0.44	0.027	0.039	0.363
36	0	0.016	0.020	0.0

octet baryon mass differences to be $\sigma_0 = 36 \pm 7$ MeV [44]. Values of the matrix elements are given in the table for 3 choices of Σ and hence y . As one can see, we expect there will be a strong dependence of the cross section on the proton strangeness, y .

The spin-dependent (SD) part of the elastic χ -nucleus cross section can be written as ¹

$$\sigma_{\text{SD}} = \frac{32}{\pi} G_F^2 m_r^2 \Lambda^2 J(J+1), \quad (23)$$

where m_r is again the reduced neutralino mass, J is the spin of the nucleus,

$$\Lambda \equiv \frac{1}{J} (a_p \langle S_p \rangle + a_n \langle S_n \rangle), \quad (24)$$

and

$$a_p = \sum_q \frac{\alpha_{2q}}{\sqrt{2}G_f} \Delta_q^{(p)}, \quad a_n = \sum_i \frac{\alpha_{2q}}{\sqrt{2}G_f} \Delta_q^{(n)}. \quad (25)$$

The factors $\Delta_q^{(N)}$ parametrize the quark spin content of the nucleon and are only significant for the light (u,d,s) quarks. A combination of experimental and theoretical results tightly constrain the linear combinations [45]

$$a_3^{(p)} \equiv \Delta_u^{(p)} - \Delta_d^{(p)} = 1.2695 \pm 0.0029 \quad (26)$$

and [46,47]

$$a_8^{(p)} \equiv \Delta_u^{(p)} + \Delta_d^{(p)} - 2\Delta_s^{(p)} = 0.585 \pm 0.025. \quad (27)$$

However, the individual $\Delta_q^{(N)}$ are relatively poorly constrained; using the recent COMPASS result [48],

$$\Delta_{rms}^{(p)} = -0.09 \pm 0.01 \text{ (stat.)} \pm 0.02 \text{ (syst.)} \approx -0.09 \pm 0.03, \quad (28)$$

where we have conservatively combined the statistical and systematic uncertainties, we may express $\Delta_{u,d}^{(N)}$ as follows in terms of known quantities [49]:

$$\Delta_u^{(p)} = \frac{1}{2} (a_8^{(p)} + a_3^{(p)}) + \Delta_s^{(p)} = 0.84 \pm 0.03 \quad (29)$$

$$\Delta_d^{(p)} = \frac{1}{2} (a_8^{(p)} - a_3^{(p)}) + \Delta_s^{(p)} = -0.43 \pm 0.03 \quad (30)$$

¹ As with the SI cross section, this expression applies in the zero momentum transfer limit and requires an additional form factor for finite momentum transfer. This form factor may have a small but non-zero dependence on a_p and a_n .

The above two uncertainties and that of $\Delta_s^{(p)}$, however, are correlated and one should instead use the independent quantities $a_3^{(p)}$ and $a_8^{(p)}$ when appropriate. The proton and neutron scalar matrix elements are related by an interchange of Δ_u and Δ_d , or

$$\Delta_u^{(n)} = \Delta_d^{(p)}, \quad \Delta_d^{(n)} = \Delta_u^{(p)}, \quad \text{and} \quad \Delta_s^{(n)} = \Delta_s^{(p)}. \quad (31)$$

In addition to the uncertainties stemming from $\Sigma_{\pi N}$, it is important to bear in mind the astrophysical uncertainties inherent in direct detection experiments. Direct and indirect detection signals are proportional to the product of the local dark matter density ρ_0 and the elastic cross section. Since the local dark matter density has not been directly measured, it is typically inferred from galactic dynamics and N -body simulations. By convention, experimental results are often presented for a neutralino density of 0.3 GeV/cm^3 , with the implicit understanding that the following significant uncertainties exist in this value. In the case of a smooth distribution of galactic dark matter, ρ_0 is estimated to be $0.2\text{-}0.4 \text{ GeV/cm}^3$ [50,51] for a spherical halo, but it may be somewhat higher, up to 0.7 GeV/cm^3 [52,53], for an elliptical halo; see Ref. [51] for a discussion of the difficulties in determining this value. Models of the galaxy based upon hierarchical formation [54], which do not assume a strictly smooth distribution of dark matter as do the above estimates, suggest that the local density may be as low as 0.04 GeV/cm^3 , but that 0.2 GeV/cm^3 is a more reasonable lower limit. One should also allow for the possibility that there may be some additional source of cold dark matter, such as axions, in which case the neutralino density would be less than ρ_0 .

As noted earlier, regions in the $m_{1/2}, m_0$ plane with fixed $\tan\beta$ for which the relic density takes on values compatible with the WMAP determined cold dark matter density, form thin strips due to co-annihilations or rapid s-channel annihilations. As a consequence, for fixed $\tan\beta$, we can adjust m_0 as a function of $m_{1/2}$ and calculate the elastic scattering cross section as a function of $m_{1/2}$. Fig. 5 [49] shows the cross sections along the WMAP-allowed strips of the $(m_{1/2}, m_0)$ planes for $\tan\beta = 10$ and 50 [22, 23, 55]. Shown are both the spin dependent cross section for $\chi - p$ and $\chi - n$ scattering (upper curves) and the spin independent cross section (lower curves, which are nearly superimposed at this scale).

The SI cross sections for χ -proton ($\sigma_{\chi p, \text{SI}}$) and χ -neutron ($\sigma_{\chi n, \text{SI}}$) scattering are typically very close, within $\sim 5\%$ of each other; close enough that they are virtually indistinguishable in Fig. 5. Likewise, the spin-dependent χ -proton ($\sigma_{\chi p, \text{SD}}$) and χ -neutron ($\sigma_{\chi n, \text{SD}}$) scattering cross sections are similar, differing by at most a factor of 2 or 3. In general, the SD χ -nucleon cross section is much larger than the SI one, by $\mathcal{O}(10^2 - 10^3)$ or more. However, we recall that the SI cross section for scattering off a nucleus, Eq. 18, contains a factor of the number of nucleons squared, whereas the SD cross section, Eq. 23, is proportional to the square of the spin, which does not grow with increasing nuclear mass. Consequently, heavy elements such as Ge and Xe are actually more sensitive to SI couplings than to SD couplings.

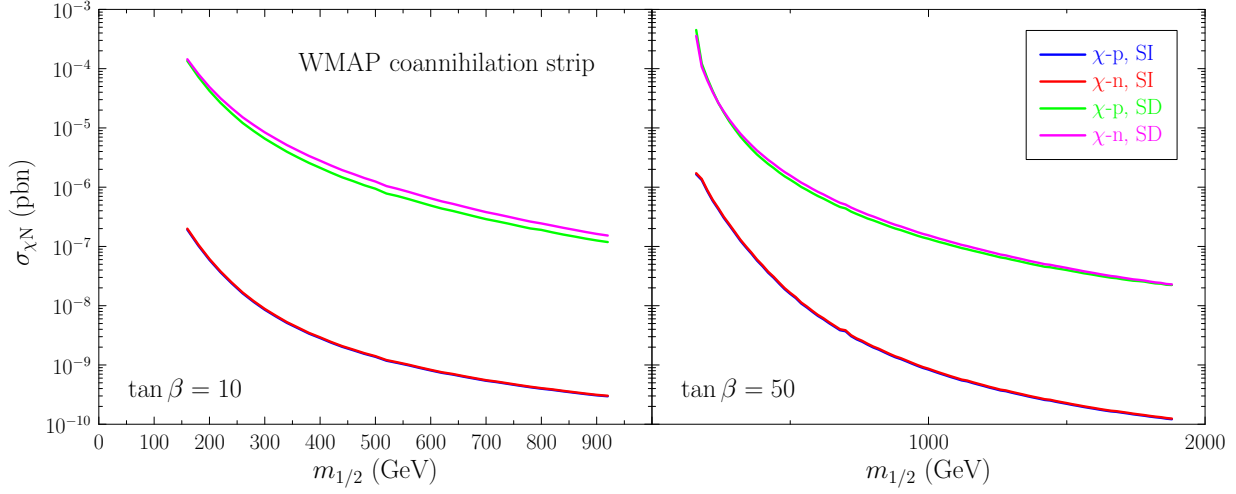


Fig. 5. The neutralino-nucleon scattering cross sections along the WMAP-allowed coannihilation strip for $\tan\beta = 10$ (left panel) and coannihilation/funnel strip for $\tan\beta = 50$ (right panel)

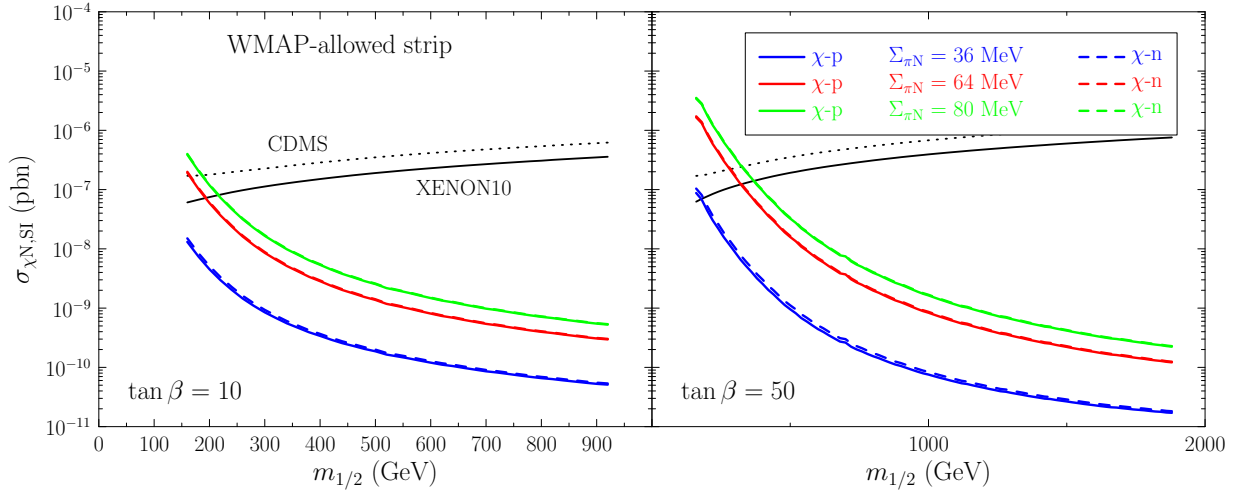


Fig. 6. The spin-independent neutralino-nucleon scattering cross section ratio along the WMAP-allowed strips for $\tan\beta = 10$ (left panel) and $\tan\beta = 50$ (right panel) for several values of $\Sigma_{\pi N}$. Experimental constraints from CDMS [56] and XENON10 [57] are also shown.

In Fig. 6, the SI cross sections are shown along the WMAP allowed coannihilation strip for $\tan\beta = 10$ and coannihilation/funnel strip for $\tan\beta = 50$ for the $\Sigma_{\pi N}$ reference values of 36 MeV (no strange scalar contribution), 64 MeV (central value), and 80 MeV (2- σ upper bound) [49]. The CDMS [56] and XENON10 [57] limits are also given. A factor of ~ 10 variation occurs in $\sigma_{\chi N, SI}$ over these $\Sigma_{\pi N}$ reference values for any given model along the WMAP strip.

Such large variations present difficulties in using any upper limit or possible future precision measurement of $\sigma_{\chi N, SI}$ from a direct detection signal to constrain the CMSSM parameters. The present CDMS and XENON10 upper limits have (almost) no impact on the WMAP strip for $\tan\beta = 10(50)$, if one makes the very conservative assumption that $\sigma_0 = 36$ MeV ($y = 0$). On the other hand, $m_{1/2} \sim 200$ GeV would be excluded for $\tan\beta = 10$ if

$\Sigma_{\pi N} = 64$ or 80 MeV. This excluded region would extend to $m_{1/2} \sim 300$ GeV for $\tan\beta = 50$ if $\Sigma_{\pi N} = 64$ or 80 MeV. Thus, the experimental uncertainty in $\Sigma_{\pi N}$ is already impinging on the ability of the present CDMS and XENON10 results to constrain the CMSSM parameter space [49].

Looking to the future, a conjectural future measurement of $\sigma_{\chi p, SI} = 4 \times 10^{-9}$ pb would only constrain $m_{1/2}$ to the range $600 \text{ GeV} < m_{1/2} < 925 \text{ GeV}$ if $\tan\beta = 10$ and $1100 \text{ GeV} < m_{1/2} < 1400 \text{ GeV}$ if $\tan\beta = 50$, for the 1- σ $\Sigma_{\pi N}$ range of 64 ± 8 MeV. If smaller values of $\Sigma_{\pi N}$ are also considered, down to $\sigma_0 = 36$ MeV ($y = 0$), these constraints would weaken to $350 \text{ GeV} < m_{1/2} < 925 \text{ GeV}$

and $550 \text{ GeV} < m_{1/2} < 1400 \text{ GeV}$ for $\tan\beta = 10$ and 50 , respectively, ruling out only the smallest values of $m_{1/2}$ ².

In Figure 7, we show the $\Sigma_{\pi N}$ dependence of $\sigma_{\chi_{N,SI}}$ [49, 58] for three benchmark models, which are essentially the well-studied benchmark models C, L, and M [59]. All of the benchmark models lead to relic densities within the WMAP preferred range of $\Omega h^2 = 0.088 - 0.120$ [2], and satisfy most phenomenological constraints³. Points C and L are points along the coannihilation strip (at low $\tan\beta = 10$ and high $\tan\beta = 50$, respectively) where the masses of the neutralino and stau are nearly degenerate. Point M is in the funnel region where the mass of the neutralino is roughly half that of the Higgs pseudoscalar. From the minimal value for $\Sigma_{\pi N}$ ($\sigma_0 = 36 \text{ MeV}$) to the 2- σ upper bound (80 MeV), $\sigma_{\chi_{N,SI}}$ varies by more than a factor of 10 (as much as a factor of 35 for model L). At these benchmarks and in other models of interest, for larger values of $\Sigma_{\pi N}$, the majority of the contribution to f_p in Eq. 19 comes from the strange quark term, with $f_{T_s}^{(p)} \propto y \propto \Sigma_{\pi N} - \sigma_0$, so that $\sigma_{\chi_{p,SI}} \sim (\Sigma_{\pi N} - \sigma_0)^2$. Thus, the SI cross sections are particularly sensitive not just to $\Sigma_{\pi N}$ and σ_0 , but to their difference. For smaller values of $\Sigma_{\pi N}$ ($\Sigma_{\pi N} \sim \sigma_0$), the strange contribution no longer dominates, but a strong dependence of $\sigma_{\chi_{N,SI}}$ on $\Sigma_{\pi N}$ does remain.

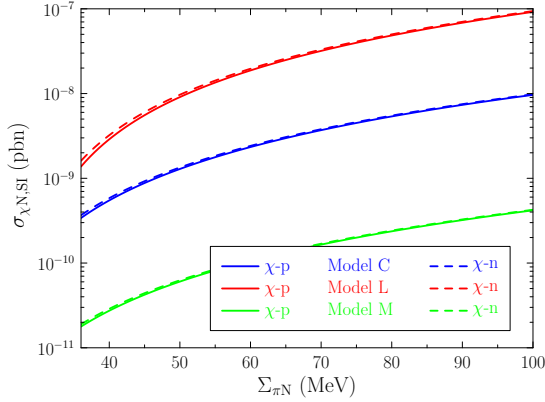


Fig. 7. The spin-independent neutralino-nucleon scattering cross section as a function of $\Sigma_{\pi N}$ for benchmark models C, L, and M. Note that $\sigma_{\chi_{p,SI}}$ and $\sigma_{\chi_{n,SI}}$ are nearly indistinguishable at the scale used in this plot.

In Fig. 8, we display the expected ranges of the spin-independent cross sections in the CMSSM when we sample randomly $\tan\beta$ as well as the other CMSSM parameters

² Moreover, as noted previously, however, detection signals only measure $\rho_0\sigma_{\chi N}$, so $\sigma_{\chi N}$ can only be determined from a signal to the precision that the local dark matter density is known.

³ The exception being a possible failure to account for the discrepancy between the theoretical and experimental results for anomalous magnetic moment of the muon [38, 39]. Points C and L are consistent with $(g-2)_\mu$, whilst the contribution from point M is too small.

[58]. All points shown satisfy all phenomenological constraints and have $\Omega_\chi h^2$ less than the WMAP upper limit. Since models with low $\Omega_\chi h^2$ can not be excluded if another form of dark matter is assumed to exist, these models have been included, but their cross sections have been scaled by a factor Ω_χ/Ω_{CDM} . In Fig. 8a, $\Sigma_{\pi N} = 45 \text{ MeV}$ has been chosen, and in 8b results for $\Sigma_{\pi N} = 64 \text{ MeV}$ are shown for comparison. As one can see, the cross sections shift higher by a factor of a few for the larger value of $\Sigma_{\pi N}$.

Also shown on the plot are the current CDMS [56], XENON10 [57] and the newest CDMS [60] exclusion curves which place an upper limit on the scattering cross section. As one can see, the current limits have only just now begun to probe CMSSM models.

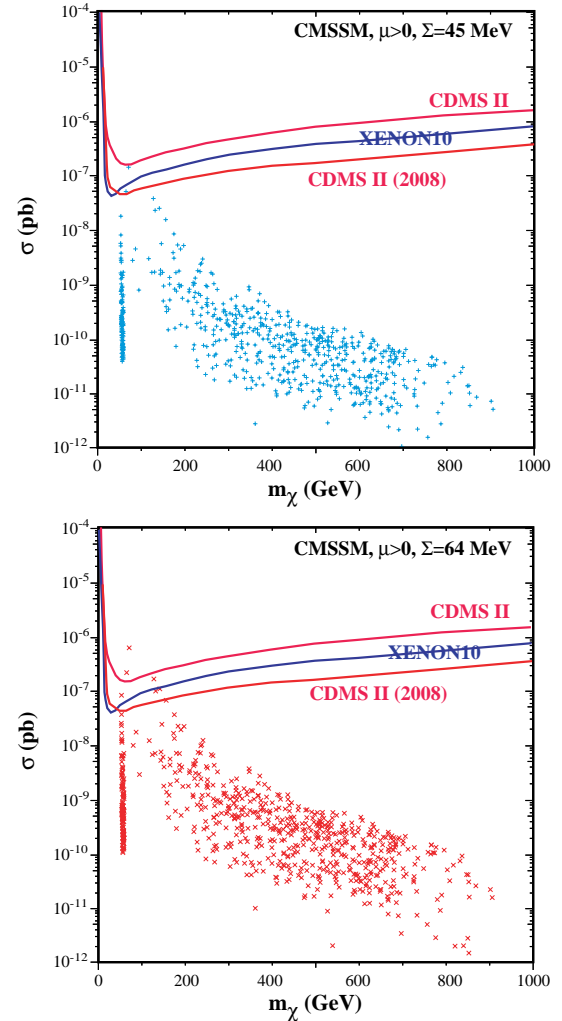


Fig. 8. Scatter plots of the spin-independent elastic-scattering cross section predicted in the CMSSM for (a) $\Sigma_{\pi N} = 45 \text{ MeV}$ and (b) 64 MeV .

5 Indirect sensitivities

Measurements of electroweak precision observables (EWPO) as well as B-physics observables (BPO) can provide interesting indirect information about the supersymmetric parameter space. We have already seen the impact of measurements of the anomalous magnetic moment of the muon, the branching ratio of $b \rightarrow s\gamma$ in addition to the non-discovery of charginos and the Higgs boson at LEP which impose significant lower bounds on $m_{1/2}$.

The following EWPO were considered in [61,62,63]: the W boson mass, M_W , the effective weak mixing angle at the Z boson resonance, $\sin^2 \theta_{\text{eff}}$, the width of the Z , Γ_Z , the Higgs mass, m_h , and $(g_\mu - 2)$ in addition to the BPO: b decays $b \rightarrow s\gamma$, $B_s \rightarrow \mu^+\mu^-$, $B_u \rightarrow \tau\nu_\tau$ and the B_s mass mixing parameter ΔM_{B_s} . An analysis was performed of the sensitivity to $m_{1/2}$ moving along the WMAP strips with fixed values of A_0 and $\tan\beta$. The experimental central values, the present experimental errors and theoretical uncertainties are as described in [63]. Assuming that the nine observables listed above are uncorrelated, a χ^2 fit has been performed with

$$\chi^2 \equiv \sum_{n=1}^7 \left[\left(\frac{R_n^{\text{exp}} - R_n^{\text{theo}}}{\sigma_n} \right)^2 + 2 \log \left(\frac{\sigma_n}{\sigma_n^{\text{min}}} \right) \right] + \chi_{m_h}^2 + \chi_{B_s}^2. \quad (32)$$

Here R_n^{exp} denotes the experimental central value of the n th observable (M_W , $\sin^2 \theta_{\text{eff}}$, Γ_Z , $(g - 2)_\mu$ and $\text{BR}(b \rightarrow s\gamma)$, $\text{BR}(B_u \rightarrow \tau\nu_\tau)$, ΔM_{B_s}), R_n^{theo} is the corresponding MSSM prediction and σ_n denotes the combined error. Additionally, σ_n^{min} is the minimum combined error over the parameter space of each data set, and $\chi_{m_h}^2$ and $\chi_{B_s}^2$ denote the χ^2 contribution coming from the experimental limits on the lightest MSSM Higgs boson mass and on $\text{BR}(B_s \rightarrow \mu^+\mu^-)$, respectively [63].

As examples of contributions to χ^2 , predictions of some of the electroweak and B-physics observables are shown in Figures 9 -14 taken from [63]. The current status of the MSSM prediction and the experimental resolution is shown in each figure. For each value of $A_0/m_{1/2}$, we plot two sets of points. For each $m_{1/2}$, m_0 is chosen to lie in the co-annihilation strip (low values of m_0) or the focus point region (high values of m_0).

The CMSSM predictions for M_W in the coannihilation and focus-point regions shown in Fig. 9 are quite similar, and depend little on A_0 . We also see that small values of $m_{1/2}$ are slightly preferred, reflecting the familiar fact that the experimental value of M_W is currently somewhat higher than the SM prediction.

The corresponding results for $\sin^2 \theta_{\text{eff}}$ in the CMSSM are shown in Fig. 10 for $\tan\beta = 10$ as functions of $m_{1/2}$. Best agreement occurs at large $m_{1/2}$ values. However, taking all uncertainties into account, the deviation for $m_{1/2}$ generally stays below the level of one sigma. We note that the predictions for $\sin^2 \theta_{\text{eff}}$ in the coannihilation and focus-point regions are somewhat different.

The predictions for m_h in the CMSSM for $\tan\beta = 10$ are shown in Fig. 11. The predicted values of m_h are similar in the coannihilation and focus-point regions. They

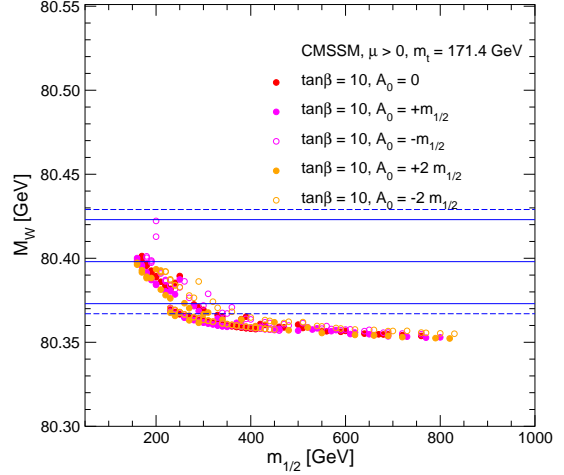


Fig. 9. The CMSSM predictions for M_W are shown as functions of $m_{1/2}$ along the WMAP strips for $\tan\beta = 10$ for various A_0 values. The centre (solid) line is the present central experimental value, and the (solid) outer lines show the current $\pm 1\text{-}\sigma$ range. The dashed lines correspond to the full error including also parametric and intrinsic uncertainties.

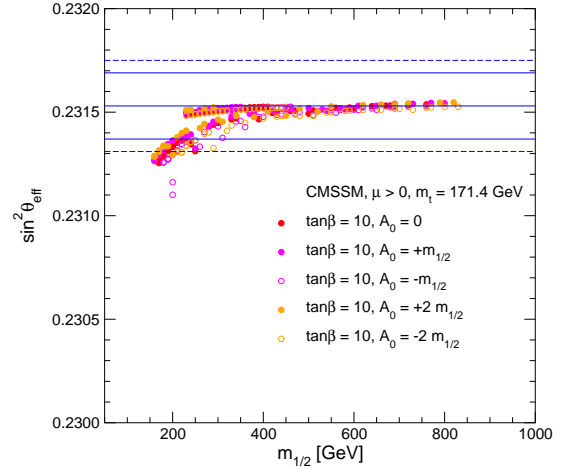


Fig. 10. The CMSSM predictions for $\sin^2 \theta_{\text{eff}}$ as functions of $m_{1/2}$ along the WMAP strips for $\tan\beta = 10$ for various A_0 values. The centre (solid) line is the present central experimental value, and the (solid) outer lines show the current $\pm 1\text{-}\sigma$ range. The dashed lines correspond to the full error including also parametric and intrinsic uncertainties.

depend significantly on A_0 , particularly in the coannihilation region, where negative values of A_0 tend to predict very low values of m_h that are disfavoured by the LEP direct search. Also shown in Fig. 11 is the present nominal 95 % C.L. exclusion limit for a SM-like Higgs boson, namely 114.4 GeV [34], and a hypothetical LHC measurement of $m_h = 116.4 \pm 0.2$ GeV.

The current status of the CMSSM prediction and the experimental resolution for the anomalous magnetic moment of the muon, Δa_μ is shown in Fig. 12, where the 1- and 2- σ bands are shown. We note that the coannihilation

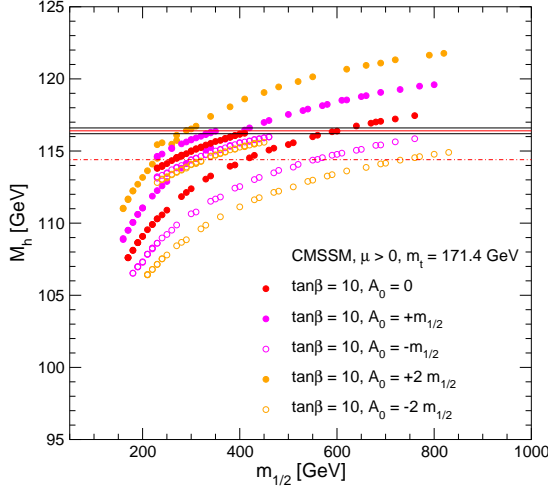


Fig. 11. The CMSSM predictions for m_h as functions of $m_{1/2}$ with $\tan\beta = 10$ for various A_0 . We also show the present 95% C.L. exclusion limit of 114.4 GeV and a hypothetical LHC measurement of $m_h = 116.4 \pm 0.2$ GeV.

and focus-point region predictions for a_μ are quite different. For $\tan\beta = 10$, the focus-point prediction agrees less well with the data.

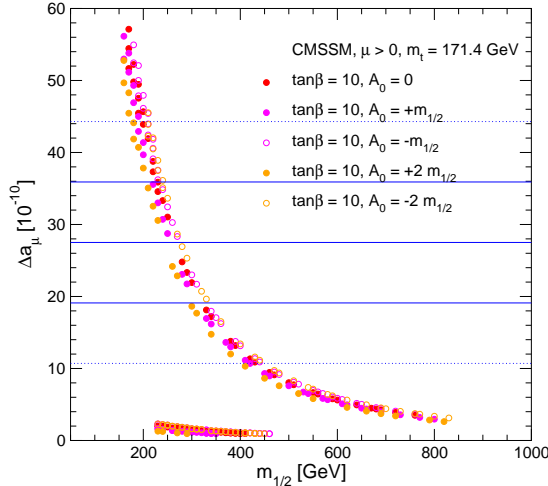


Fig. 12. The CMSSM predictions for $(g-2)_\mu$, Δa_μ , as functions of $m_{1/2}$ along the WMAP strips for $\tan\beta = 10$ for various A_0 values. In each panel, the centre (solid) line is the present central experimental value, and the solid (dotted) outer lines show the current $\pm 1(2)$ - σ ranges.

Next we turn to some B-physics observables. In Fig. 13 we show the predictions in the CMSSM for $BR(b \rightarrow s\gamma)$ for $\tan\beta = 10$ as functions of $m_{1/2}$, compared with the 1- σ experimental error (full line) and the full error (dashed line, but assuming a negligible parametric error). We see that positive values of A_0 are disfavoured at small $m_{1/2}$.

Finally, in Fig. 14 the CMSSM predictions for $BR(B_s \rightarrow \mu^+\mu^-)$ for $\tan\beta = 10$ as functions of $m_{1/2}$ are compared

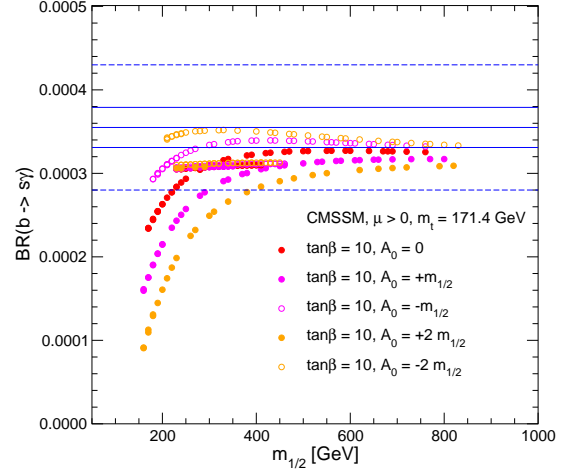


Fig. 13. The CMSSM predictions for $BR(b \rightarrow s\gamma)$ as functions of $m_{1/2}$ along the WMAP strips for $\tan\beta = 10$ and various choices of A_0 . The central (solid) line indicates the current experimental central value, and the other solid lines show the current ± 1 - σ experimental range. The dashed line is the ± 1 - σ error including also the full intrinsic error.

with the present Tevatron limit. For $\tan\beta = 10$, the CMSSM prediction is significantly below the present and future Tevatron sensitivity. However, already with the current sensitivity, the Tevatron starts to probe the CMSSM coannihilation region for $\tan\beta = 50$ (not shown) and $A_0 \geq 0$, whereas the CMSSM prediction in the focus-point region is significantly below the current sensitivity.

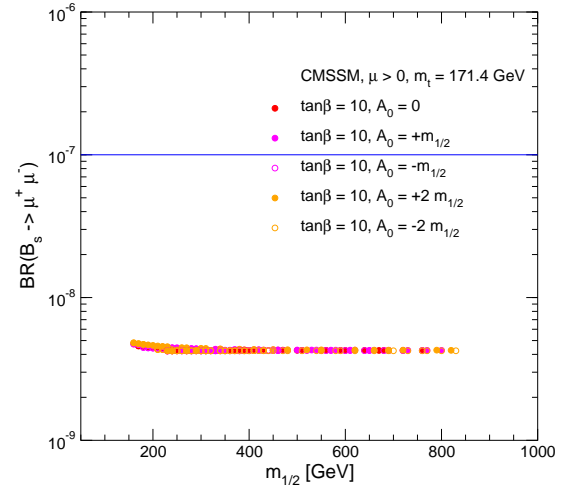


Fig. 14. The CMSSM predictions for $BR(B_s \rightarrow \mu^+\mu^-)$ as functions of $m_{1/2}$ along the WMAP strips for $\tan\beta = 10$ and various choices of A_0 . The solid line indicates the current experimental 95% C.L. exclusion bound.

In Fig. 15 the net result of the χ^2 analysis in the CMSSM is shown using the combined χ^2 values for the EWPO and BPO, computed from Eq. 32. We see that the global minimum of $\chi^2 \sim 4.5$ for both values of $\tan\beta$.

This is quite a good fit for the number of experimental observables being fitted. For both values of $\tan\beta$, the focus-point region is disfavoured by comparison with the coannihilation region, though this effect is less important for $\tan\beta = 50$. For $\tan\beta = 10$, $m_{1/2} \sim 300$ GeV and $A_0 > 0$ are preferred, whereas, for $\tan\beta = 50$, $m_{1/2} \sim 600$ GeV and $A_0 < 0$ are preferred. This change-over is largely due to the impact of the LEP m_h constraint for $\tan\beta = 10$ and the $b \rightarrow s\gamma$ constraint for $\tan\beta = 50$.

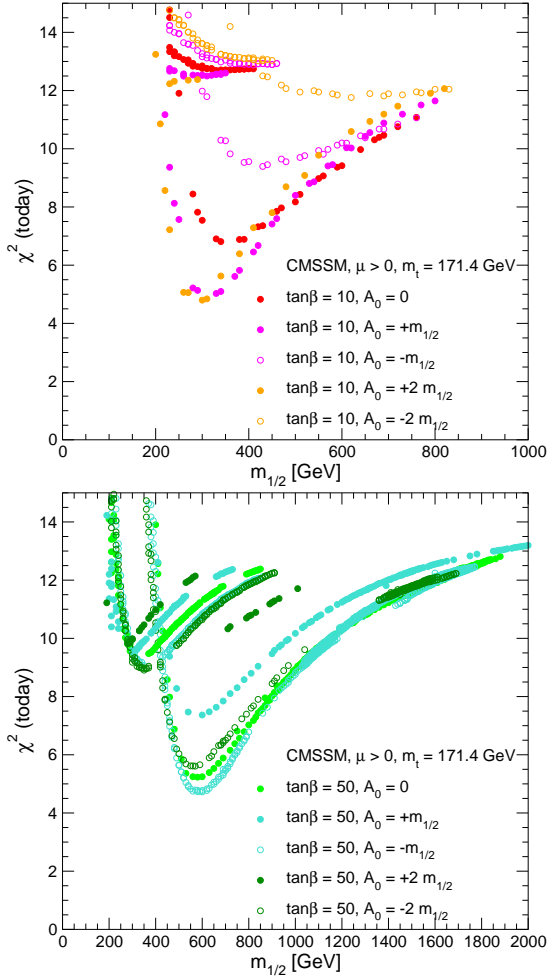


Fig. 15. The combined χ^2 function for the electroweak observables M_W , $\sin^2\theta_{\text{eff}}$, Γ_Z , $(g-2)_\mu$, m_h , and the b physics observables $\text{BR}(b \rightarrow s\gamma)$, $\text{BR}(B_s \rightarrow \mu^+\mu^-)$, $\text{BR}(B_u \rightarrow \tau\nu_\tau)$ and ΔM_{B_s} , evaluated in the CMSSM for $\tan\beta = 10$ (a) and $\tan\beta = 50$ (b) for various discrete values of A_0 . We use $m_t = 171.4 \pm 2.1$ GeV and $m_b(m_b) = 4.25 \pm 0.11$ GeV, and m_0 is chosen to yield the central value of the cold dark matter density indicated by WMAP and other observations for the central values of m_t and $m_b(m_b)$.

6 GUT-less models

The input scale at which universality is assumed in CMSSM models is usually taken to be the SUSY GUT scale, $M_{GUT} \sim$

2×10^{16} GeV. However, it may be more appropriate in some models to assume the soft SUSY-breaking parameters to be universal at some different input scale, M_{in} . Specific scenarios in which the soft SUSY-breaking parameters may be universal at a scale below M_{GUT} occur in models with mixed modulus-anomaly mediated SUSY breaking, also called mirage-mediation [64], and models with warped extra dimensions [65]. In the case of mirage-mediation, the universality scale is the mirage messenger scale, which is predicted to be $M_{in} \sim 10^{10} - 10^{12}$ GeV in the case of KKLT-style moduli stabilization [66]. In other models, the universality scale may lie anywhere between 1 TeV and M_{Pl} .

In the CMSSM with universality imposed at the GUT scale, the one-loop renormalizations of the gaugino masses M_a , where $a = 1, 2, 3$, are the same as those for the corresponding gauge couplings, α_a . Thus, at the one-loop level the gaugino masses at any scale $Q \leq M_{GUT}$ is given in Eq. 15 with $t = Q$. On the other hand, in a GUT-less CMSSM, where the gauge-coupling strengths run at all scales below the GUT scale but the soft SUSY-breaking parameters run only below the lower universality scale, M_{in} , at which all the gaugino masses are assumed to equal to $m_{1/2} = M_a(M_{in})$, we have

$$M_a(Q) = \frac{\alpha_a(Q)}{\alpha_a(M_{in})} m_{1/2} \quad (33)$$

at the one-loop level. Since the runnings of the coupling strengths in GUT and GUT-less CMSSM scenarios are identical, the low-energy effective soft gaugino masses, $M_a(Q)$, in GUT-less cases are less separated and closer to $m_{1/2}$ than in the usual GUT CMSSM. This is seen in Fig. 16 where the low energy gaugino masses are shown as a function of the input unification scale.

Similarly, the sfermion masses also run less and have masses closer to m_0 at the weak scale than their corresponding masses in the CMSSM. The soft SUSY-breaking scalar masses are renormalized by both gauge and (particularly in the cases of third-generation sfermions) Yukawa interactions, so the running is somewhat more complicated. At the one-loop level one can summarize the effects of renormalizations at any $Q \leq M_{in}$ as

$$m_{0_i}^2(Q) = m_0^2(M_{in}) + C_i(Q, M_{in}) m_{1/2}^2, \quad (34)$$

where we make the CMSSM assumption that the $m_0^2(M_{in})$ are universal at M_{in} , and the $C_i(Q, M_{in})$ are renormalization coefficients that vanish as $Q \rightarrow M_{in}$. The two-loop-renormalized soft SUSY-breaking masses of the first- and second-generation left- and right-handed squarks, $\tilde{q}_{L,R}$, the stop mass eigenstates, $\tilde{t}_{1,2}$, and the left- and right-handed sleptons, $\tilde{\ell}_{L,R}$ are shown in Fig. 17. We see again that in GUT-less cases the soft SUSY-breaking scalar masses are less separated and closer to m_0 than in the usual GUT-scale CMSSM.

One of the most dramatic changes when M_{in} is lowered from the GUT scale is its effect on the footprint in the $(m_{1/2}, m_0)$ plane of the constraint on the relic abundance of neutralinos inferred from WMAP. In the GUT-

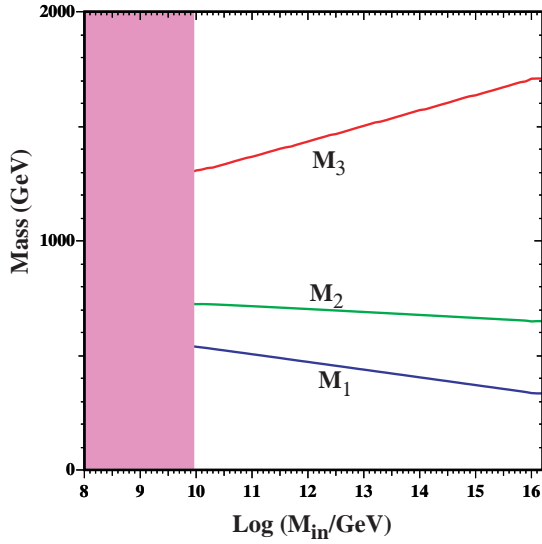


Fig. 16. The dependences of observable gaugino mass parameters on the input scale M_{in} at which they are assumed to be universal. The calculations are made for the representative case $m_{1/2} = 700$ GeV, $m_0 = 1000$ GeV, $A_0 = 0$, $\tan\beta = 10$ and $\mu > 0$.

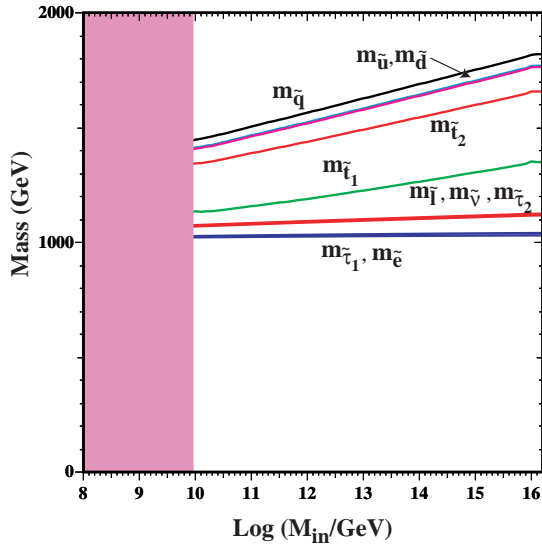


Fig. 17. As in Fig. 16, the dependences of observable scalar mass parameters on the input scale M_{in} at which they are assumed to be universal.

less CMSSM scenario [28], as the universality scale is lowered to $M_{in} \sim 10^{12}$ GeV, the co-annihilation strip, the funnel and the focus point regions of the CMSSM approach each other and merge, forming a small WMAP-preferred island in a sea of parameter space where the neutralino relic density is too small to provide all the cold dark matter wanted by WMAP.

For comparison purposes, the CMSSM plane for $\tan\beta = 10$ is shown in Fig. 18. There are already changes in the relic density as the universality scale is lowered to $M_{in} =$

10^{14} GeV seen in Fig. 19. The allowed focus-point region starts to separate from the LEP chargino bound, moving to larger $m_{1/2}$. For $M_{in} = 10^{13}$ GeV, the allowed focus-point region also dips further down, away from the electroweak vacuum condition boundary, while the coannihilation strip moves up and farther away from the region where the stau is the LSP. This is shown in Fig. 20. Another remarkable feature at this value of M_{in} is the appearance of the rapid-annihilation funnel, familiar in the GUT-scale CMSSM at large $\tan\beta$, but an unfamiliar feature for $\tan\beta = 10$.

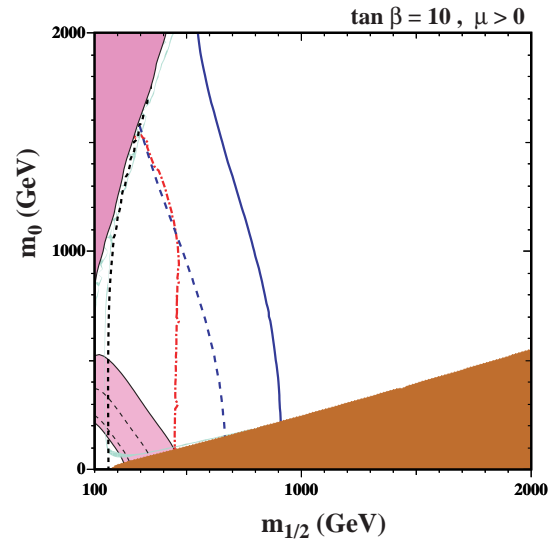
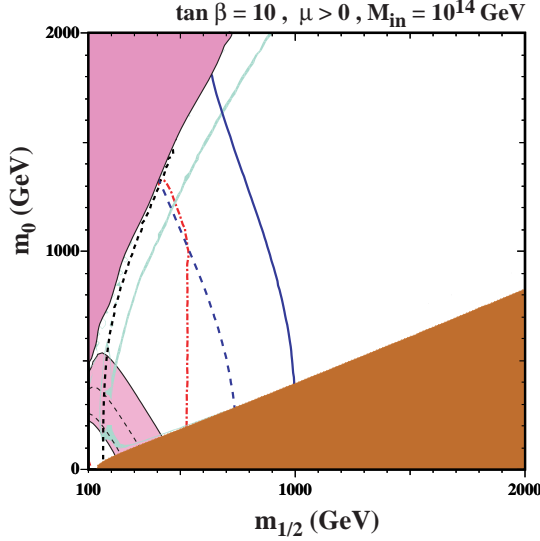
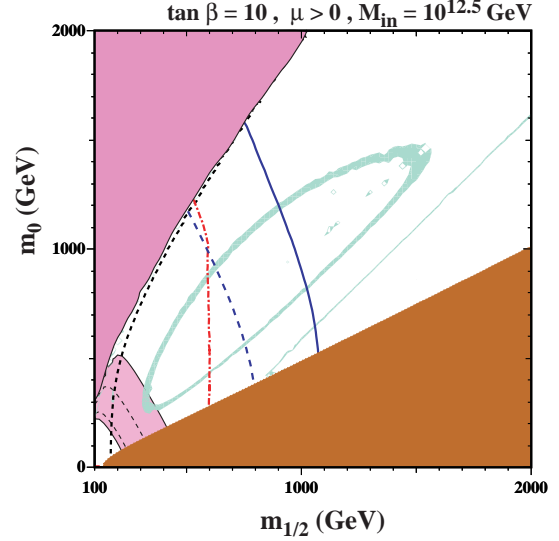
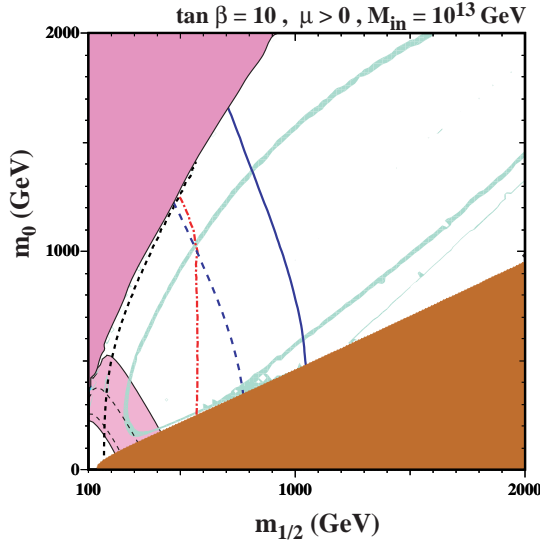
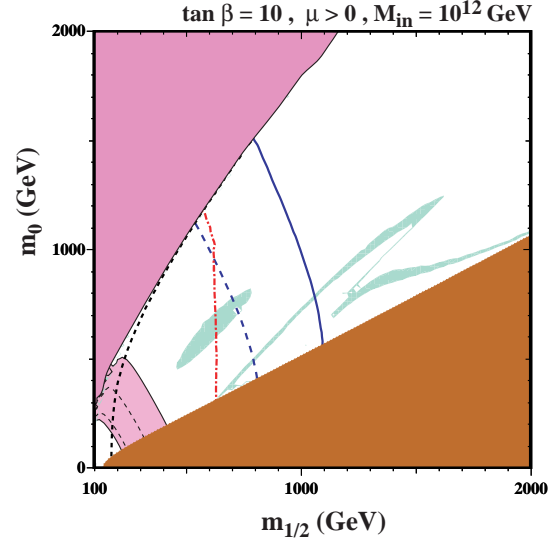


Fig. 18. The $(m_{1/2}, m_0)$ plane with $\tan\beta = 10$ and $A_0 = 0$ for $M_{in} = M_{GUT}$. We show contours representing the LEP lower limits on the chargino mass (black dashed line), and the Higgs bound (red dot-dashed). We also show the region ruled out because the LSP would be charged (dark red shading), and that excluded by the electroweak vacuum condition (dark pink shading). The region favoured by WMAP has light turquoise shading, and the region suggested by $g_\mu - 2$ at $2\text{-}\sigma$ has medium (pink) shading, with the $1\text{-}\sigma$ contours shown as black dashed lines. The solid (dashed) dark blue contours correspond to the approximate sparticle reach with 10 (1.0) fb^{-1} of integrated LHC luminosity, as discussed in the text.

As the universality scale is further decreased to $M_{in} = 10^{12.5}$ GeV, as shown in panel Fig. 21, the atoll formed by the conjunction of what had been the focus-point and coannihilation strips has shrunk, so that it lies entirely within the range of $(m_{1/2}, m_0)$ shown in the figure. We now see clearly two distinct regions of the plane excluded due to an excess relic density of neutralinos; the area enclosed by the atoll and the slice between the lower funnel wall and the boundary of the already-excluded $\tilde{\tau}$ -LSP region.

In Fig. 22 for $M_{in} = 10^{12}$ GeV, the focus-point and coannihilation regions are fully combined and the atoll has mostly filled in to become a small island of acceptable relic density. To the right of this island is a strip that is pro-

Fig. 19. As in Fig. 18 for $M_{in} = 10^{14}$ GeV.Fig. 21. As in Fig. 18 for $M_{in} = 10^{12.5}$ GeV.Fig. 20. As in Fig. 18 for $M_{in} = 10^{13}$ GeV.Fig. 22. As in Fig. 18 for $M_{in} = 10^{12}$ GeV.

vided by the lower funnel wall. The strip curves slightly as $m_{1/2}$ increases then takes a sharp plunge back down towards the boundary of the region where the stau is the LSP, a feature associated with the $\chi\chi \rightarrow h + A$ threshold. Reduction in the universality scale from this point results in the lower funnel wall being pushed down into the excluded $\tilde{\tau}$ LSP region and total evaporation of the island as seen in Figs. 23 and 24 and only a small residual turquoise region at large $m_{1/2}$ where the relic density is within the WMAP limits. At all other points in the visible part of the $(m_{1/2}, m_0)$ plane the relic density of neutralinos is too low to provide fully the cold dark matter density preferred by WMAP *et al.* Of course, these SUSY models would not be excluded if there is another source of cold dark matter in the universe.

The discovery potential of ATLAS was examined in [67], and more recently a CMS analysis [68] has provided reach contours in the $(m_0, m_{1/2})$ plane within the CMSSM for $\tan\beta = 10$. Both studies found that the greatest discovery potential is achieved by an inclusive analysis of the channel with missing transverse energy, E_T^{miss} , and three or more jets. To a good approximation, the contours depend only on $m_{\tilde{q}}$ and $m_{\tilde{g}}$, although processes involving other gauginos and sleptons may become important near the focus-point and coannihilation strips [69]. The 5- σ inclusive supersymmetry discovery contours in the CMSSM for 1.0 and 10 fb^{-1} of integrated LHC luminosity are shown for $\tan\beta = 10$ in Figure 13.5 of Ref. [68]. Since the inclusive reach is expected to be fairly linear above $m_0 = 1.5$ TeV, these contours have been extended [70]

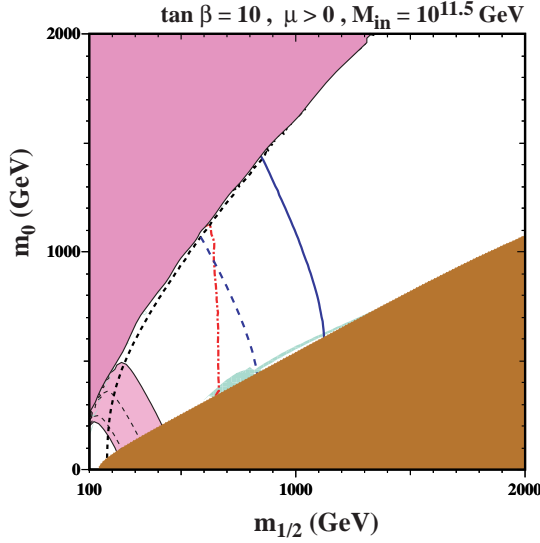


Fig. 23. As in Fig. 18 for $M_{in} = 10^{11.5}$ GeV.

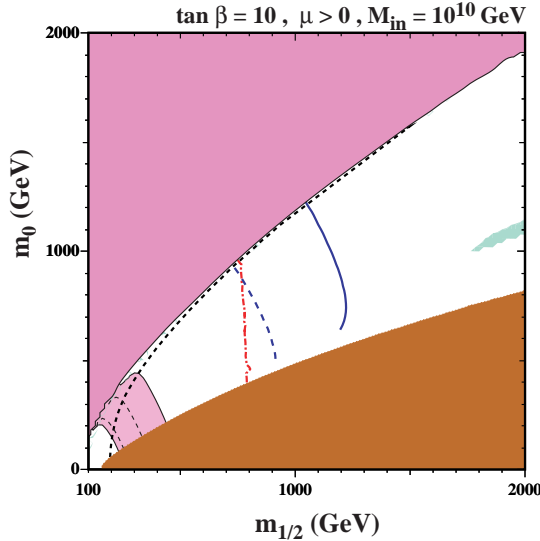


Fig. 24. As in Fig. 18 for $M_{in} = 10^{10}$ GeV.

linearly above $m_0 = 1200$ GeV, then the sensitivity was fit with a third-order polynomial in m_0 and $m_{1/2}$ to extend the approximate LHC supersymmetry reach out to $m_0 = 2$ TeV, as shown in Fig. 25. These fits are compared with the CMS reaches. The largest differences between the approximate reach contours and the contours shown in the CMS TDR [68] are ~ 25 GeV for the 10 fb^{-1} contour and ~ 50 GeV for the 1 fb^{-1} contour.

The next step is to change variables from $(m_{1/2}, m_0) \rightarrow (m_{\tilde{g}}, m_{\tilde{q}})$ using (33) and (34). Starting from the contours specified in Fig. 25 as functions of the gluino and squark masses, for each value of M_{in} , the discovery contours were translated [70] back into the corresponding $(m_{1/2}, m_0)$ plane. Clearly, the contours move as the universality scale M_{in} is lowered and the gluino and squark masses change

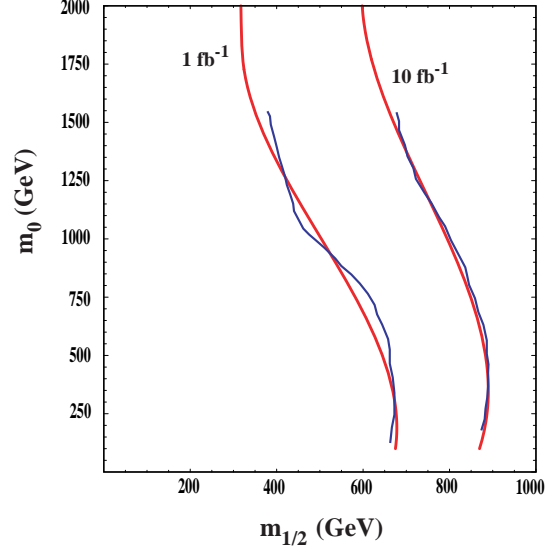


Fig. 25. Approximate LHC supersymmetry reach contours for integrated luminosities of 1 fb^{-1} and 10 fb^{-1} (smooth curves), compared with the expected CMS reach given in the CMS TDR [68] for $\tan \beta = 10$ [70].

according to (33) and (34). The shifted contours are displayed appropriately in Figs. 18 - 24, showing the change in the reach across the $m_{1/2}, m_0$ plane with respect to the regions preferred cosmologically.

7 mSUGRA models

As discussed earlier, mSUGRA models, in contrast to the CMSSM, have an additional boundary condition, namely the value of the bilinear B -term is fixed at the GUT scale to $B_0 = A_0 - m_0$. As a consequence, one is no longer free to choose a fixed value of $\tan \beta$ across the $m_{1/2} - m_0$ plane. Instead, $\tan \beta$ is derived for each value of $m_{1/2}, m_0$ and A_0 [26]. Phenomenologically distinct planes are rather determined by a choice for A_0/m_0 . In Fig. 26, two such planes are shown with (a) $A_0/m_0 = 3 - \sqrt{3}$ as predicted in the simplest model of supersymmetry breaking [27] and with (b) $A_0/m_0 = 2.0$. Shown are the contours of $\tan \beta$ (solid blue lines) in the $(m_{1/2}, m_0)$ planes. Also shown are the contours where $m_{\chi^\pm} > 104$ GeV (near-vertical black dashed lines) and $m_h > 114$ GeV (diagonal red dash-dotted lines). The regions excluded by $b \rightarrow s\gamma$ have medium (green) shading, and those where the relic density of neutralinos lies within the WMAP range have light (turquoise) shading. The region suggested by $g_\mu - 2$ at $2\text{-}\sigma$ has very light (pink) shading. As one can see, relatively low values of $\tan \beta$ are obtained across the planes.

Another difference between the CMSSM and models based on mSUGRA concerns the mass of the gravitino. In the CMSSM, it is not specified and can be taken suitably large so that the neutralino is the LSP (outside the stau LSP region). In mSUGRA, the scalar masses at the GUT scale, m_0 , are determined by (and equal to) the

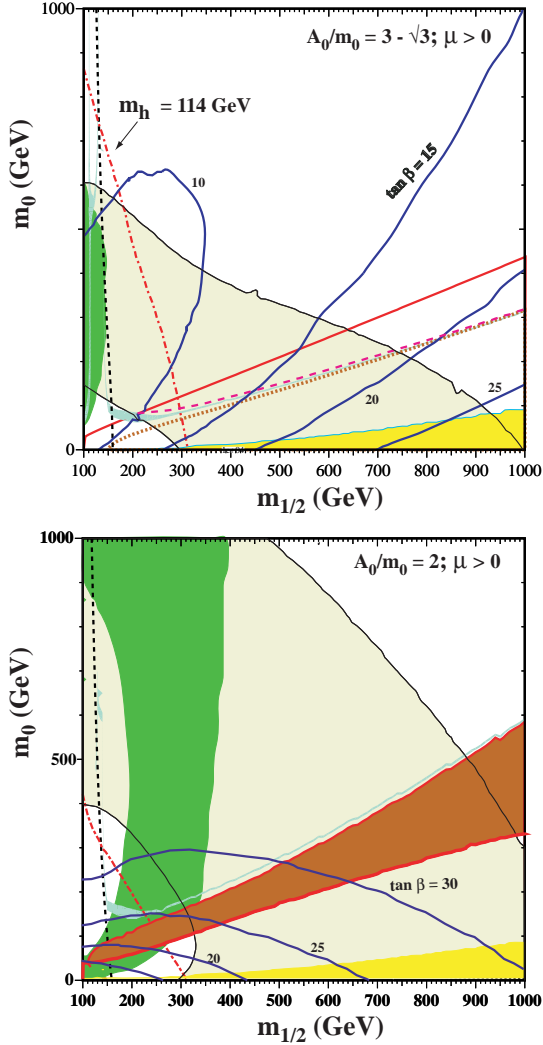


Fig. 26. Examples of $mSUGRA$ $(m_{1/2}, m_0)$ planes with contours of $\tan\beta$ superposed, for $\mu > 0$ and (a) the simplest Polonyi model with $A_0/m_0 = 3 - \sqrt{3}$, and (b) $A_0/m_0 = 2.0$, all with $B_0 = A_0 - m_0$. In each panel, we show the regions excluded by the LEP lower limits on MSSM particles and those ruled out by $b \rightarrow s\gamma$ decay (medium green shading): the regions favoured by $g_\mu - 2$ are very light (yellow) shaded, bordered by a thin (black) line. The dark (chocolate) solid lines separate the gravitino LSP regions. The regions favoured by WMAP in the neutralino LSP case have light (turquoise) shading. The dashed (pink) line corresponds to the maximum relic density for the gravitino LSP, and regions allowed by BBN constraint neglecting the effects of bound states on NSP decay are light (yellow) shaded.

gravitino mass. In Fig. 26, the gravitino LSP and the neutralino LSP regions are separated by dark (chocolate) solid lines. Above this line, the neutralino (or stau) is the LSP, whilst below it, the gravitino is the LSP [71]. As one can see by comparing the two panels, the potential for neutralino dark matter in $mSUGRA$ models is dependent on A_0/m_0 . In panel (a), the only areas where the neutralino density are not too large occur where the Higgs mass is far

too small or, at higher m_0 the chargino mass is too small. At larger A_0/m_0 , the co-annihilation strip rises above the neutralino-gravitino delineation. In panel (b), we see the familiar co-annihilation strip. It should be noted that the focus point region is not realized in $mSUGRA$ models as the value of μ does not decrease with increasing m_0 when A_0/m_0 is fixed and $B_0 = A_0 - m_0$. There are also no funnel regions, as $\tan\beta$ is never sufficiently high.

In the gravitino LSP regions, the next-to-lightest supersymmetric particle (NSP) may be either the neutralino or stau which is now unstable. The relic density of gravitinos is acceptably low only below the dashed (pink) line. This excludes a supplementary domain of the $(m_{1/2}, m_0)$ plane in panel (a) which has a neutralino NSP (the dotted (red) curve in panel (a) separates the neutralino and stau NSP regions). However, the strongest constraint is provided by the effect of neutralino or stau decays on big bang nucleosynthesis (BBN) [72]. Outside the light (yellow) shaded region, the decays spoil the success of BBN. Note that in panel (b), there remains a region which is excluded because the stau is the LSP.

Recently, new attention has been focussed on the regions with a stau NSP due to its ability to form bound states (primarily with ${}^4\text{He}$). When such bound states occur, they catalyze certain nuclear reactions such as ${}^4\text{He}(D, \gamma){}^6\text{Li}$ which is normally highly suppressed due to the production of a low energy γ whereas the bound state reaction is not [73]. In Fig. 27a, the $(m_{1/2}, m_0)$ plane is displayed showing explicit element abundance contours [74] when the gravitino mass is $m_{3/2} = 0.2m_0$ in the *absence* of stau bound state effects. To the left of the solid black line the gravitino is the not the LSP. The diagonal red dotted line corresponds to the boundary between a neutralino and stau NSP. Above the line, the neutralino is the NSP, and below it, the NSP is the stau. Very close to this boundary, there is a diagonal brown solid line. Above this line, the relic density of gravitinos from NSP decay is too high, i.e.,

$$\frac{m_{3/2}}{m_{NSP}} \Omega_{NSP} h^2 > 0.12. \quad (35)$$

Thus we should restrict our attention to the area below this line.

The very thick green line labelled ${}^7\text{Li} = 4.3$ corresponds to the contour where ${}^7\text{Li}/\text{H} = 4.3 \times 10^{-10}$, a value very close to the standard BBN result for ${}^7\text{Li}/\text{H}$. It forms a ‘V’ shape, whose right edge runs along the neutralino-stau NSP border. Below the V, the abundance of ${}^7\text{Li}$ is smaller than the standard BBN result. However, for relatively small values of $m_{1/2}$, the ${}^7\text{Li}$ abundance does not differ very much from this standard BBN result: it is only when $m_{1/2} \gtrsim 3000$ GeV that ${}^7\text{Li}$ begins to drop significantly. The stau lifetime drops with increasing $m_{1/2}$, and when $\tau \sim 1000$ s, at $m_{1/2} \sim 4000$ GeV, the ${}^7\text{Li}$ abundance has been reduced to an observation-friendly value close to 2×10^{-10} as claimed in [75] and shown by the (unlabeled) thin dashed (green) contours.

The region where the ${}^6\text{Li}/{}^7\text{Li}$ ratio lies between 0.01 and 0.15 forms a band which moves from lower left to upper right. As one can see in the orange shading, there is

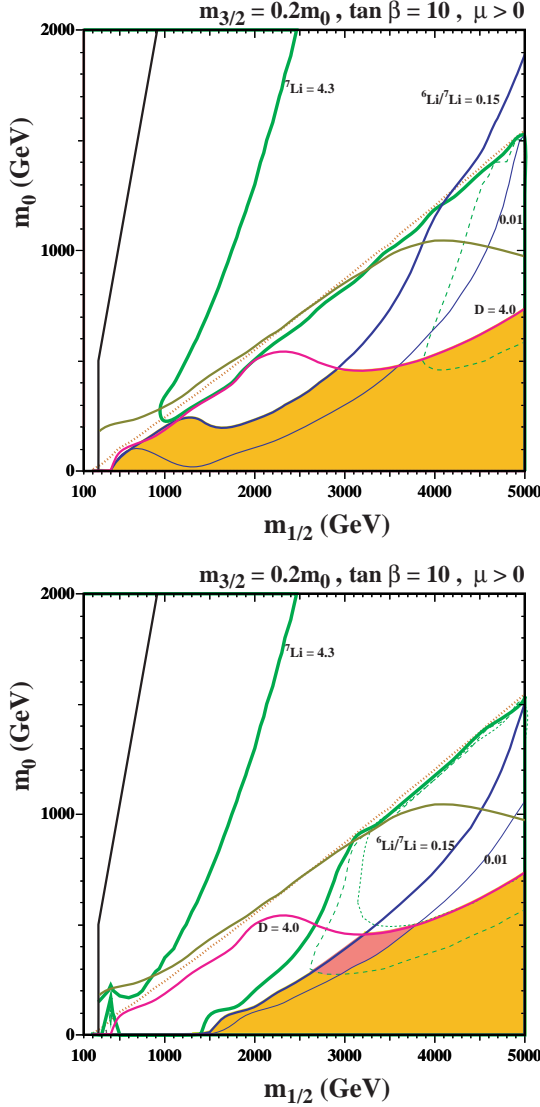


Fig. 27. The $(m_{1/2}, m_0)$ planes for $A_0 = 0$, $\mu > 0$ and $\tan\beta = 10$ with $m_{3/2} = 0.2m_0$ without (a) and with (b) the effects of bound states included. The regions to the left of the solid black lines are not considered, since there the gravitino is not the LSP. In the orange (light) shaded regions, the differences between the calculated and observed light-element abundances are no greater than in standard BBN without late particle decays. In the pink (dark) shaded region in panel b, the abundances lie within the ranges favoured by observation. The significances of the other lines and contours are explained in the text.

a large region where the lithium isotopic ratio can be made acceptable. However, if we restrict to $D/H < 4.0 \times 10^{-5}$, we see that this ratio is interesting only when ${}^7\text{Li}$ is at or slightly below the standard BBN result.

Turning now to Fig. 27b, we show the analogous results when the bound-state effects are included in the calculation. The abundance contours are identical to those in panel (a) above the diagonal dotted line, where the NSP is a neutralino and bound states do not form. We also note

that the bound state effects on D and ${}^3\text{He}$ are quite minimal, so that these element abundances are very similar to those in Fig. 27a. However, comparing panels (a) and (b), one sees dramatic bound-state effects on the lithium abundances. Everywhere to the left of the solid blue line labeled 0.15 is excluded. In the stau NSP region, this means that $m_{1/2} \gtrsim 1500$ GeV. Moreover, in the stau region to the right of the ${}^6\text{Li}/{}^7\text{Li} = 0.15$ contour, the ${}^7\text{Li}$ abundance drops below 9×10^{-11} (as shown by the thin green dotted curve). In this case, not only do the bound-state effects increase the ${}^6\text{Li}$ abundance when $m_{1/2}$ is small (i.e., at relatively long stau lifetimes), but they also decrease the ${}^7\text{Li}$ abundance when the lifetime of the stau is about 1500 s. Thus, at $(m_{1/2}, m_0) \simeq (3200, 400)$, we find that ${}^6\text{Li}/{}^7\text{Li} \simeq 0.04$, ${}^7\text{Li}/\text{H} \simeq 1.2 \times 10^{-10}$, and $D/\text{H} \simeq 3.8 \times 10^5$. Indeed, when $m_{1/2}$ is between 3000-4000 GeV, the bound state effects cut the ${}^7\text{Li}$ abundance roughly in half. In the darker (pink) region, the lithium abundances match the observational plateau values, with the properties ${}^6\text{Li}/{}^7\text{Li} > 0.01$ and $0.9 \times 10^{-10} < {}^7\text{Li}/\text{H} < 2.0 \times 10^{-10}$.

Next we return to an example of an mSUGRA model based on the Polonyi model for which $A_0/m_0 = 3 - \sqrt{3}$ with the condition that $m_{3/2} = m_0$. In Fig. 28a, we show the mSUGRA model without the bound states. In the upper part of the plane, we do not have gravitino dark matter. We see that ${}^3\text{He}/\text{D}$ [76] eliminates all but a triangular area which extends up to $m_0 = 1000$ GeV, when $m_{1/2} = 5000$ GeV. Below the ${}^3\text{He}/\text{D} = 1$ contour, D and ${}^7\text{Li}$ are close to their standard BBN values, and there is a substantial orange shaded region. We note that ${}^6\text{Li}$ is interestingly high, between 0.01 and 0.15 in much of this region.

As seen in Fig. 28b, when bound-state effects are included in this mSUGRA model, both lithium isotope abundances are too large except in the extreme lower right corner, where there is a small region shaded orange. However, there is no region where the lithium abundances fall within the favoured plateau ranges.

The prospects for direct detection in the mSUGRA models (when the neutralino is the LSP) is very similar to that of the CMSSM but slightly more difficult. In a plot such as that shown in Fig. 8, the mSUGRA predictions are down by a factor of about 2 or less.

8 The NUHM

In the NUHM, the Higgs soft masses are treated independently from m_0 . In effect, this allows one to choose μ and the Higgs pseudoscalar mass, m_A freely (up to phenomenological constraints). Two examples of planes in the NUHM are shown in Figs. 29 and 30. In Fig. 29, an $m_{1/2} - m_0$ plane is shown with $\mu = 700$ GeV and $m_A = 400$ GeV fixed across the plane [30]. As usual, the light (turquoise) shaded area is the cosmologically preferred region. There is a bulk region satisfying this preference at $m_{1/2} \sim 150$ GeV to 350 GeV and $m_0 \sim 100$ GeV. The dark (red) shaded regions are excluded because a charged sparticle is lighter than the neutralino. As in the

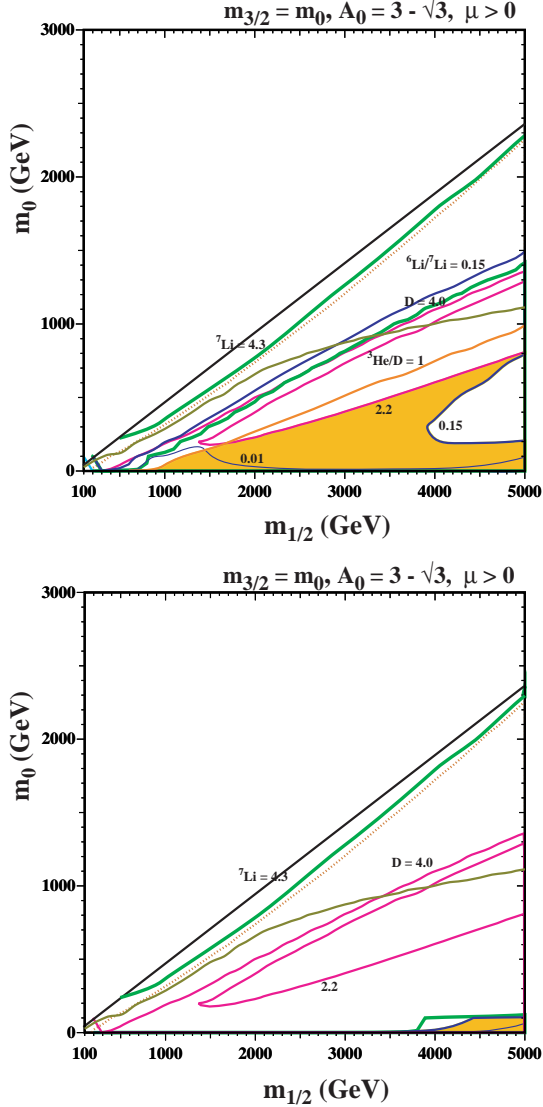


Fig. 28. As in Fig. 27, for the $mSUGRA$ case with $A_0/m_0 = 3 - \sqrt{3}$.

CMSSM, there are light (turquoise) shaded strips close to these forbidden regions where coannihilation suppresses the relic density sufficiently to be cosmologically acceptable. Further away from these regions, the relic density is generally too high. At small $m_{1/2}$ and m_0 the left handed sleptons, and also the sneutrinos, become lighter than the neutralino. The darker (dark blue) shaded area is where a sneutrino is the LSP.

The near-vertical dark (black) dashed and light (red) dot-dashed lines in Fig. 29 are the LEP exclusion contours $m_{\chi_{\pm}} > 104$ GeV and $m_h > 114$ GeV respectively. As in the CMSSM case, they exclude low values of $m_{1/2}$, and hence rule out rapid relic annihilation via direct-channel h and Z^0 poles. The solid lines curved around small values of $m_{1/2}$ and m_0 bound the light (pink) shaded region favoured by a_μ and recent analyses of the e^+e^- data.

A striking feature in Fig. 29 when $m_{1/2} \sim 450$ GeV is a strip with low $\Omega_\chi h^2$, which has bands with acceptable relic density on either side. The low- $\Omega_\chi h^2$ strip is due to rapid annihilation via the direct-channel A, H poles which occur when $m_\chi = m_A/2 = 200$ GeV, indicated by the near-vertical solid (blue) line. These correspond to the funnel regions found in the CMSSM [19,21], but at larger $\tan\beta$. At higher $m_{1/2} \sim 1300-1400$ GeV, there is another region of acceptable relic density. This band, the transition band, is broadened because the neutralino acquires significant Higgsino content as $m_{1/2}$ becomes greater than μ , and the relic density is suppressed by the increased W^+W^- production. To the right of this band, the relic density falls below the WMAP value.

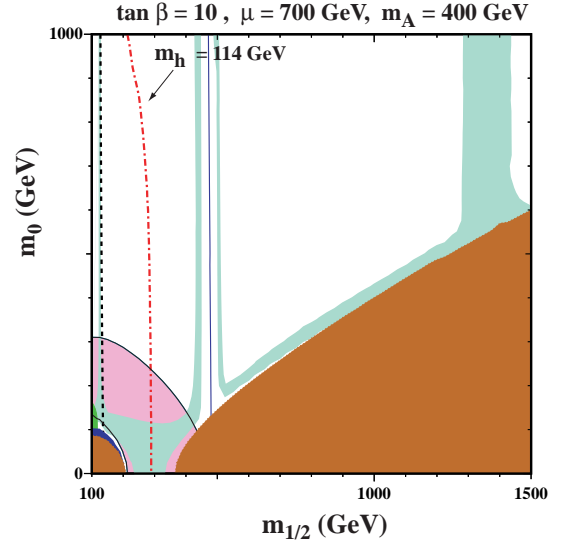


Fig. 29. Projections of the NUHM model on the $(m_{1/2}, m_0)$ planes for $\tan\beta = 10$ and $\mu = 700$ GeV and $m_A = 400$ GeV. The (red) dot-dashed lines are the contours $m_h = 114$ GeV as calculated using FeynHiggs [35], and the near-vertical (black) dashed lines are the contours $m_{\chi_{\pm}} = 104$ GeV. The light (turquoise) shaded areas are the cosmologically preferred regions. The dark (brick red) shaded regions is excluded because a charged particle is lighter than the neutralino, and the darker (dark blue) shaded regions is excluded because the LSP is a sneutrino. There is a very small medium (green) shaded region excluded by $b \rightarrow s\gamma$, at small $m_{1/2}$. The regions allowed by the E821 measurement of a_μ at the 2- σ level, are shaded (pink) and bounded by solid black lines.

Another example of an NUHM plane is shown in Fig. 30, representing a $\mu - m_A$ plane with a fixed choice of values of $\tan\beta = 35$, $m_{1/2} = 500$ GeV, $m_0 = 1000$ GeV and $A_0 = 0$ [58]. Line types and shading are as in Fig. 29. The region with acceptable relic density now takes the form of a narrow strip of values of $\mu \sim \pm 300 \rightarrow 350$ GeV where the relic density lies within the WMAP range for almost all values of m_A . The exception is a narrow strip centred on $m_A \sim 430$ GeV, namely the rapid-annihilation funnel where $m_\chi \sim m_A/2$, which would be acceptable if

there is some other source of cold dark matter. Note the increased importance of the $b \rightarrow s\gamma$ constraint which now excludes almost all of $\mu < 0$.

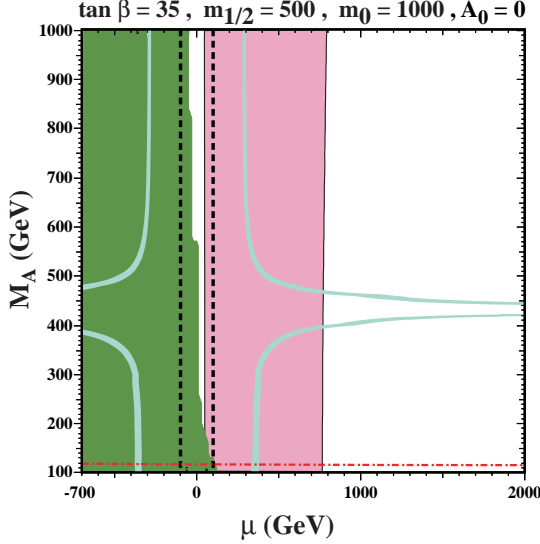


Fig. 30. As in 29, for the $\mu - m_A$ plane with $m_{1/2} = 500$ GeV, $m_0 = 1000$ GeV, $\tan \beta = 35$ and $A_0 = 0$. Here note that the constraint from $b \rightarrow s\gamma$ excludes most of $\mu < 0$.

An interesting representation of the NUHM parameter space is found in the construction of a $(M_A, \tan \beta)$ plane. A generic $(M_A, \tan \beta)$ plane for fixed $m_{1/2} = 600$ GeV, $m_0 = 800$ GeV, $\mu = 1000$ GeV and $A_0 = 0$ [77, 78] is shown in Fig. 31. The relic LSP density satisfies the WMAP constraint only in narrow, near-vertical (pale blue) shaded strips crossing the plane. These lie to either side of the vertical (purple) line where $m_\chi = M_A/2$. Within the narrow unshaded strip straddling this line, the relic density is suppressed by rapid direct-channel annihilations to a value below the lower limit of the range for the cold dark matter density indicated by WMAP et al. This entire strip would be acceptable for cosmology if there were some additional component of cold dark matter. Outside the shaded WMAP-compatible strips, at both larger and smaller values of M_A , the relic LSP density is too high, and these regions are unacceptable. The LEP lower limit on m_h excludes a strip of this plane at low M_A and/or $\tan \beta$ indicated by the dash-dotted (red) line. In addition, a_μ (pink shading) prefers relatively large $\tan \beta > 36$, while $b \rightarrow s\gamma$ excludes a (green shaded) region at low M_A and $\tan \beta$.

It is clear from this example and the properties found in the $\mu - m_A$ plane discussed above, that one can construct a $m_A - \tan \beta$ plane such that (nearly) the entire plane respects the cosmological relic density constraint [63, 78]. For example, from Fig. 31 we see that if one adjusts $m_{1/2}$ continuously as a function of M_A so as to remain within one of the narrow WMAP strips as M_A increases we can cover the entire $m_A - \tan \beta$ plane. Alternatively, we can use Fig. 30 as a guide to construct $m_A - \tan \beta$ planes as well. Fixing μ in the range of 250 -

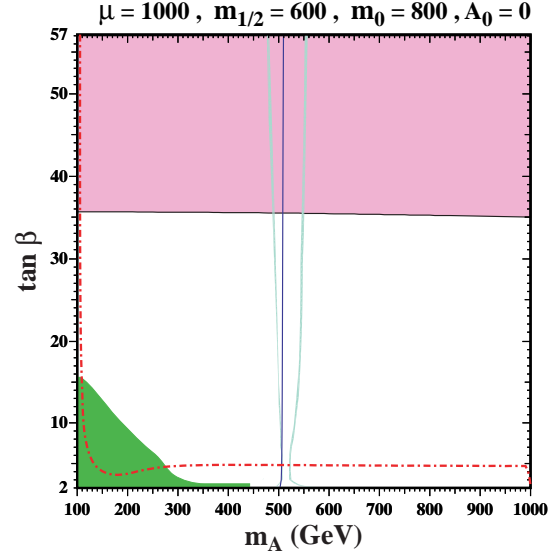


Fig. 31. A $(M_A, \tan \beta)$ plane with $m_{1/2} = 600$ GeV, $m_0 = 800$ GeV, $\mu = 1000$ GeV and $A_0 = 0$. The range of cold dark matter density preferred by WMAP and other observations is attained in two narrow (pale blue) strips, one on either side of the vertical solid (blue) line where $m_\chi = M_A/2$. The dark (green) shaded region at low M_A and low $\tan \beta$ is excluded by $b \rightarrow s\gamma$, and the medium (pink) shaded region at $\tan \beta > 36$ is favoured by a_μ . The region below the (red) dot-dashed line is excluded by the LEP bounds on m_h .

400 GeV will allow us to obtain a good relic density over the entire $m_A - \tan \beta$ plane except for the strip centered on $m_\chi = M_A/2$. These planes can be used as particularly useful benchmarks for existing and future searches for Higgs bosons [78]. We will consider two such planes which will be referred to as planes P1 and P3.

The plane P1 is defined by fixed $\mu = 1000$ GeV and $m_0 = 800$ GeV, while P3 is defined by fixed $m_{1/2} = 500$ GeV and $m_0 = 1000$ GeV. As one can see, the light shaded (turquoise) region now fills up each plane except for a vertical swath in P3 where s-channel annihilation through m_A drives the relic density to small values. A likelihood analysis of these NUHM benchmark surfaces, including the EWPO M_W , $\sin^2 \theta_{\text{eff}}$, Γ_Z , $(g-2)_\mu$ and m_h and the BPO $\text{BR}(b \rightarrow s\gamma)$, $\text{BR}(B_s \rightarrow \mu^+ \mu^-)$, $\text{BR}(B_u \rightarrow \tau \nu_\tau)$ and ΔM_{B_s} was performed recently in [63]. The lowest χ^2 value in plane P1 (P3) is $\chi^2_{\text{min}} = 7.1(7.4)$ and the corresponding best-fit point is shown by a (red) cross in Fig. 32 as are the $\Delta\chi^2 = 2.30$ and 4.61 contours around the best-fit point. The (black shaded) region in the lower left is excluded at the 95 % C.L. by the LEP Higgs searches in the channel $e^+ e^- \rightarrow Z^* \rightarrow Zh, H$ [34].

The planes shown in Fig. 32 also show the 5- σ discovery contours for $b\bar{b} \rightarrow H/A \rightarrow \tau^+ \tau^-$ at the LHC, where the τ 's decay to jets and electrons or muons. The analysis is based on 60 fb^{-1} for the final state $\tau^+ \tau^- \rightarrow \text{jets}$ [79] and on 30 fb^{-1} for the $\tau^+ \tau^- \rightarrow e + \text{jet}$ [80] and $\tau^+ \tau^- \rightarrow \mu + \text{jet}$ [81] channels, collected with the CMS detector. As shown in [82], the impact of the supersymmetric param-

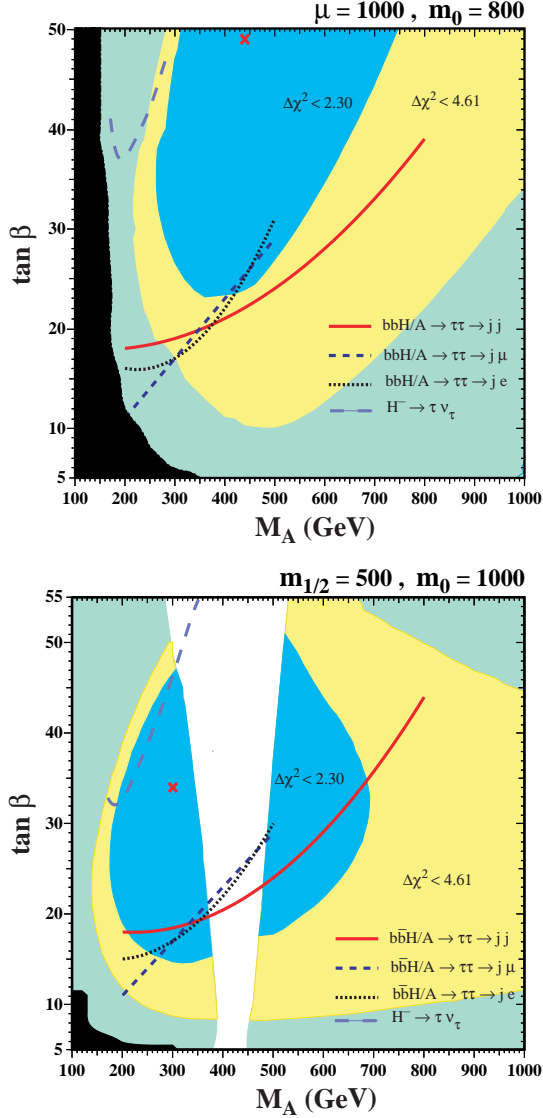


Fig. 32. The $(M_A, \tan\beta)$ planes for the NUHM benchmark surfaces P1 and P3, displaying the contours of $\Delta\chi^2$ found in a recent global fit to EWPO and BPO [63]. All surfaces have $A_0 = 0$. The dark shaded (black) region corresponds to the parameter region that is excluded by the LEP Higgs searches. Also shown are the 5- σ discovery contours for $H/A \rightarrow \tau^+\tau^-$ at the LHC with 60 or 30 fb^{-1} (depending on the τ decay channels) and for $H^\pm \rightarrow \tau^\pm\nu$ detection in the CMS detector when $M_{H^\pm} > m_t$

eters other than M_A and $\tan\beta$ on the discovery contours is relatively small in this channel. We see that the whole $\Delta\chi^2 < 2.30$ regions of the surface P1 would be covered by the LHC $H/A \rightarrow \tau^+\tau^-$ searches, and most of the corresponding regions of the surface P3.

We also show in Fig. 32 the 5- σ contours for discovery of the H^\pm via its $\tau^\pm\nu$ decay mode at the LHC, in the case $M_{H^\pm} > m_t$. We see that the coverage is limited in each of the scenarios P1 and P3 to $M_A < 300$ GeV and $\tan\beta > 30$, reaching a small part of the $\Delta\chi^2 < 2.30$ region

of surface P3, and only a small part of the $\Delta\chi^2 < 4.61$ region of surface P1. One may also search for $H^\pm \rightarrow \tau^\pm\nu$ for lighter $M_{H^\pm} < m_t$, but in the cases of surfaces P1 this would be useful only in the regions already excluded by LEP, and the accessible regions in surfaces P3 would also be quite limited.

In Fig. 33 the current reach of the XENON10 experiment [57] is shown on planes P1 and P3. The solid line in the figure correspond to the XENON10 bound obtained assuming $\Sigma_{\pi N} = 45$ MeV. The corresponding reach obtained if $\Sigma_{\pi N} = 64$ MeV is shown by the dotted curve. In plane P1, the current reach is minimal and does not enter the $\Delta\chi^2 < 4.61$ region, whereas for plane P3 the best fit point would already have been probed by the XENON10 experiment if $\Sigma_{\pi N} = 64$ MeV. If the strangeness content of the proton were zero, it would correspond to $\Sigma_{\pi N} = 36$ MeV, and the XENON10 reach in this case is displayed by the dashed curve. Finally, we note that a future sensitivity to a cross section of 10^{-8} pb would cover the entire surface in P3 while in P1 would only extend slightly past the $\Sigma_{\pi N} = 64$ MeV curve.

As can be inferred from the benchmark surface shown above, in the NUHM, current constraints already exclude many interesting models [58]. These models generically have large scattering cross sections. Scatter plots of showing the reach of CDMS and XENON10 for both $\Sigma_{\pi N} = 45$ MeV and 64 MeV are shown in Fig. 34. In comparison with Fig. 8, one sees that many more viable models are already currently being probed.

9 A Hint of Higgs

The CDF and D0 Collaborations have already established important limits on the (heavier) MSSM Higgs bosons, particularly at large $\tan\beta$ [83,84,85,86,87]. Recently the CDF Collaboration, investigating the channel

$$p\bar{p} \rightarrow \phi \rightarrow \tau^+\tau^-, \quad (\phi = h, H, A), \quad (36)$$

has been unable to improve these limits to the extent of the sensitivity expected with the analyzed integrated luminosity of $\sim 1 \text{ fb}^{-1}$ [86], whereas there is no indication of any similar effect in D0 data [87]. Within the MSSM the channel (36) is enhanced as compared to the corresponding SM process by roughly a factor of $\tan^2\beta / ((1 + \Delta_b)^2 + 9)$ [88], where Δ_b includes loop corrections to the $\phi b\bar{b}$ vertex (see [88] for details) and is subdominant for the $\tau^+\tau^-$ final state. Correspondingly, the unexpected weakness of the CDF exclusion might be explicable within the MSSM if $m_A \approx 160$ GeV and $\tan\beta \gtrsim 45$.

In the CMSSM, there are no parameter sets consistent with all the experimental and theoretical constraints. In particular, low values of $m_{1/2}$ are required to obtain low values of m_A . For $m_A \simeq 160$ GeV and the other parameters tuned to fulfill the B physics constraints, there are no CMSSM solutions for which the lightest Higgs mass is not in direct contradiction with experimental limits [34]. However, we do find that all the constraints may be satisfied in the NUHM [89,90].

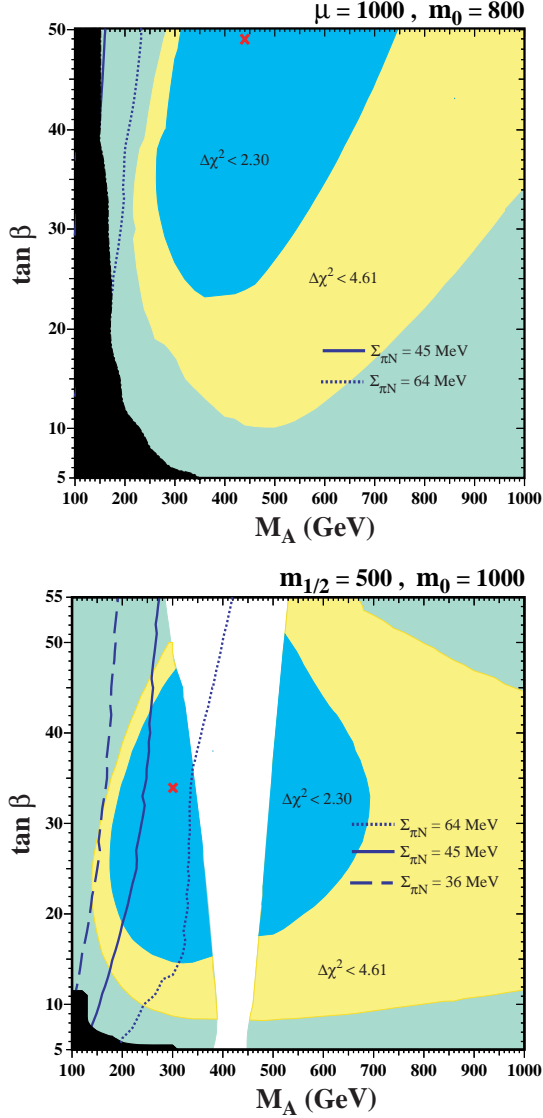


Fig. 33. The same $(M_A, \tan \beta)$ planes for the NUHM benchmark surfaces (a) P1 and (b) P3 as in Fig. 32, displaying the expected sensitivities of present direct searches for the scattering of dark matter particles.

We consider first the $(m_{1/2}, m_0)$ plane shown in panel (a) of Fig. 35, which has $\tan \beta = 45$, $\mu = 370$ GeV and $A_0 = -1800$ GeV, as well as $M_A = 160$ GeV. As before, the dark (brown) shaded region at low m_0 is forbidden, because there the LSP would be the lighter stau. The WMAP cold dark matter constraint is satisfied only within the lighter (turquoise) shaded region. To the left of this region, the relic density is too small, due to s -channel annihilation through the Higgs pseudoscalar A . As $m_{1/2}$ increases away from the pole, the relic density increases toward the WMAP range. However, as $m_{1/2}$ is increased, the neutralino acquires a larger Higgsino component and annihilations to pairs of W and Z bosons become enhanced. To the right of this transition region, the relic density again lies below the WMAP preferred

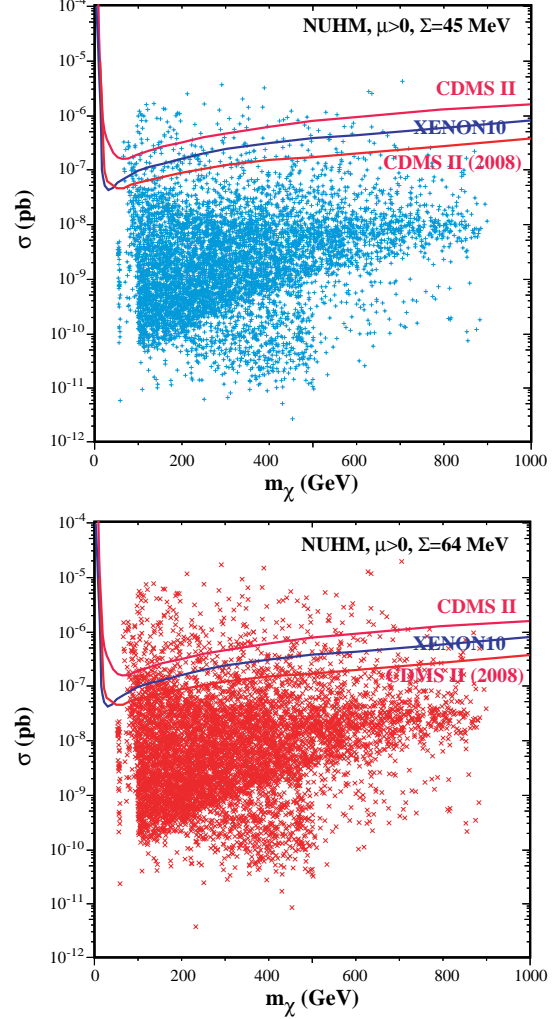


Fig. 34. Scatter plots of the spin-independent elastic-scattering cross section predicted in the NUHM (a) for $\Sigma_{\pi N} = 45$ MeV (b) and 64 MeV.

value. The shaded region here is therefore an overlap of the funnel and transition regions discussed in [30]. The $\text{BR}(B_s \rightarrow \mu^+ \mu^-)$ constraint [91] is satisfied between the outer black dash-dotted lines, labelled 10^{-7} , representing the current limit on that branching ratio. Also shown are the contours where the branching ratio is 2×10^{-8} , close to the sensitivity likely to be attainable soon by CDF and D0. Between these two contours, there is a strong cancellation between the flavor-violating contributions arising from the Higgs and chargino couplings at the one-loop level and the Wilson coefficient counterterms contributing to $\text{BR}(B_s \rightarrow \mu^+ \mu^-)$ [77].

The dash-dotted (red) line shows the contour corresponding to $m_h = 114$ GeV, and only the region to the right of this line is compatible with the constraint imposed by m_h (it should be kept in mind that there is still a ~ 3 GeV uncertainty in the prediction of m_h [35]). Also shown in pink shading is the region favoured by $(g - 2)_\mu$ at the two- σ level. The one- and two- σ con-

tours for $(g-2)_\mu$ are shown as elliptical dashed and solid black contours, respectively. The region which is compatible with the WMAP relic density and m_h , and is also within the two- σ $(g-2)_\mu$ experimental bound, has $\text{BR}(B_s \rightarrow \mu^+\mu^-) > 2 \times 10^{-8}$. The measured value of $\text{BR}(b \rightarrow s\gamma)$ is in agreement with the theory prediction only to the left of the solid (green) region.

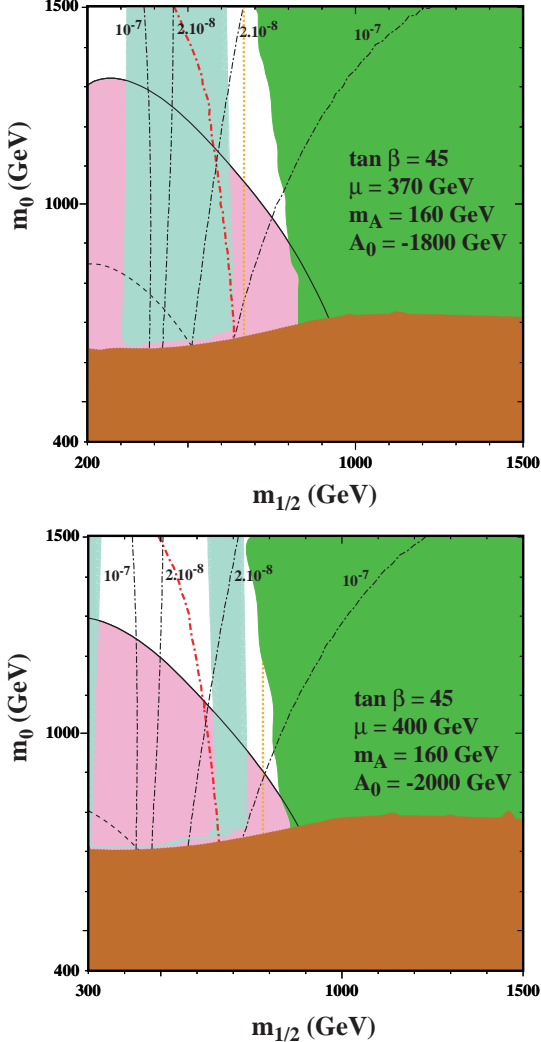


Fig. 35. The NUHM parameter space as a function of $m_{1/2}$ and m_0 for $\mu = 370(400)$ GeV and $A_0 = -1800(-2000)$ GeV in panels (a) (b). We fix $M_A = 160$ GeV, $\tan\beta = 45$, $m_t = 171.4$ GeV and $m_b = 4.25$ GeV. For the description of the various lines and shaded areas, see the text.

We see that there is a narrow wedge of allowed parameter space in Fig. 35(a), which has $m_{1/2} \sim 600$ GeV and $m_0 \sim 700$ to 1100 GeV. The $\text{BR}(b \rightarrow s\gamma)$ constraint is satisfied easily throughout this region, and $(g-2)_\mu$ cuts off the top of the wedge, which would otherwise have extended to $m_0 \gg 1500$ GeV. Within the allowed wedge, m_h is very close to the LEP lower limit, and $\text{BR}(B_s \rightarrow \mu^+\mu^-) > 2 \times 10^{-8}$. If M_A were much smaller (< 130 GeV),

there would be no wedge consistent simultaneously with the Ω_{CDM} , m_h and $\text{BR}(B_s \rightarrow \mu^+\mu^-)$ constraints.

Given the matrix element uncertainties for direct detection summarized above, we show in Fig. 35(a) the $1\text{-}\sigma$ lower limit on the calculated value of the elastic cross section as compared to the CDMS upper limit [56]. In the portion of the plane to the left of the (orange) dotted line, the lower limit on the calculated spin-independent elastic cross section is smaller than the CDMS upper bound, assuming the canonical local density. Whilst we have assumed $\Sigma_{\pi N} = 45$ MeV, the calculated lower limit effectively assumes zero strangeness contribution to the proton mass, i.e., $y = 0$. In the region of interest, the lower limit on the calculated cross section is about 80% of the CDMS upper bound, whereas with a strangeness contribution of $y = 0.2$, the cross section would exceed the CDMS bound by a factor of ~ 3 . Thus, if Nature has picked this corner of the NUHM parameter space, we expect direct detection of dark matter to be imminent. Consistency with the XENON10 limit would further require a reduction in the local dark matter density (to its lower limit). Intriguingly, the XENON10 experiment has seen some potential signal events that are, however, interpreted as background.

Panel (a) of Fig. 36 explores the (μ, A_0) plane for the choice $(m_{1/2}, m_0) = (600, 800)$ GeV, values close to the lower tip of the allowed wedge in Fig. 35(a). In this case, the region allowed by the $\text{BR}(B_s \rightarrow \mu^+\mu^-)$ constraint is *below* the upper dash-dotted black line, and the LEP m_h constraint is satisfied only *above* the dash-dotted red line. We see that only a restricted range $360 \text{ GeV} < \mu < 390$ GeV is compatible with the dark matter constraint. This corresponds to the transition strip where the neutralino is the appropriate bino/Higgsino combination. To the left of this strip, the relic density is too small and to the right, it is too large. Only a very restricted range of $A_0 \sim -1600$ GeV is compatible simultaneously with the m_h and $\text{BR}(B_s \rightarrow \mu^+\mu^-)$ constraints. Very large negative values of A_0 are excluded as the LSP is the lighter stau. On the (μ, A_0) plane, the elastic scattering cross section is a rapidly decreasing function of μ and is almost independent of A_0 . Indeed, NUHM points excluded by CDMS (or XENON10) generally have low values of μ and M_A [22]. Values of $\mu > 355$ GeV are compatible with CDMS if the strangeness contribution to the proton mass is negligible. For this choice of parameters, the entire displayed plane is compatible with $\text{BR}(b \rightarrow s\gamma)$ and $(g-2)_\mu$.

Panel (b) of Fig. 36 shows what happens if $m_{1/2}$ is increased to 700 GeV, keeping m_0 and the other inputs the same. Compared to Fig. 36(a), we see that the WMAP strip becomes narrower and shifts to larger $\mu \sim 400$ GeV, and that $\text{BR}(b \rightarrow s\gamma)$ starts to exclude a region visible at smaller μ . If $m_{1/2}$ were to be increased much further, the dark matter constraint and $\text{BR}(b \rightarrow s\gamma)$ would no longer be compatible for this value of m_0 . We also see that, by comparison with 35(a), the $\text{BR}(B_s \rightarrow \mu^+\mu^-)$ constraint has moved to lower A_0 , but the m_h constraint has dropped even further, and $m_h > 114$ GeV over the entire visible plane. The net result is a region compatible with all the constraints that extends from $A_0 \sim -1850$ GeV down to

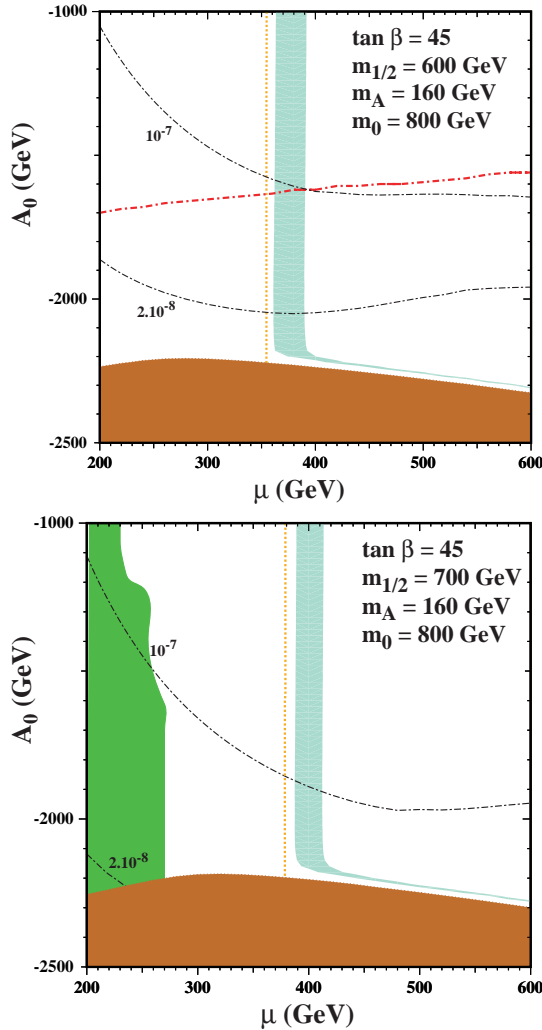


Fig. 36. The NUHM parameter space as a function of μ and A_0 for $m_{1/2} = 600(700)$ GeV and $m_0 = 800$ GeV in panels (a) (b). We fix $M_A = 160$ GeV, $\tan \beta = 45$, $m_t = 171.4$ GeV and $m_b = 4.25$ GeV. For the description of the various lines and shaded areas, see the text.

$A_0 \sim -2150$ GeV for $\mu \sim 400$ GeV, with a coannihilation filament extending to larger μ when $A_0 \sim -2200$ GeV. Once again all of the WMAP strip in this panel is compatible with CDMS.

The larger allowed area of parameter space is reflected in panel (b) of Fig. 35, which has $\mu = 400$ GeV and $A_0 = -2000$ GeV, as well as $\tan \beta = 45$ and $M_A = 160$ GeV as before. In this case, we see that a substantial region of the WMAP strip with $m_{1/2} \sim 700$ GeV and a width $\delta m_{1/2} \sim 100$ GeV, extending from $m_0 \sim 750$ GeV to higher m_0 is allowed by all the other constraints. The $\text{BR}(B_s \rightarrow \mu^+ \mu^-)$ and m_h constraints have now moved to relatively low values of $m_{1/2}$, but we still find $\text{BR}(B_s \rightarrow \mu^+ \mu^-) > 2 \times 10^{-8}$ and m_h close to the LEP lower limit. The $(g-2)_\mu$ constraint truncates the allowed region at $m_0 \sim 1050$ GeV. Once again, the allowed region is compatible with CDMS

(to the left of the (orange) dotted line) provided the strangeness contribution to the proton mass is small.

Clearly our anticipation for the discovery of supersymmetry or new physics is great. If the CDF hint of the Higgs boson is realized, we should expect to see numerous departures from the standard model including the decay of B_s to $\mu^+ \mu^-$, $\text{BR}(b \rightarrow s\gamma)$ should show deviations from the standard model value, and dark matter should be discovered by CDMS or XENON10 in the near future. Similarly if an observation of new physics in any one of these areas occurs, we should be ready for flood of new data showing departures from the standard model.

Acknowledgements

I would like to thank J. Ellis, T. Hahn, S. Heinemeyer, P. Sandick, Y. Santoso, C. Savage, V. Spanos, A. Weber, G. Weiglein for enjoyable collaborations from which this review is derived. This work was partially supported by DOE grant DE-FG02-94ER-40823.

References

1. S. M. Faber and J. J. Gallagher, *Ann. Rev. Astron. Astrophys.* **17** (1979) 135; A. Bosma, *Ap. J.* **86** (1981) 1825; V. C. Rubin, W. K. Ford and N. Thonnard, *Ap. J.* **238** (1980) 471; V. C. Rubin, D. Burstein, W. K. Ford and N. Thonnard, *Ap. J.* **289** (1985) 81; T. S. Van Albada and R. Sancisi, *Phil. Trans. R. Soc. Land.* **A320** (1986) 447; M. Persic and P. Salucci, *Ap. J. Supp.* **99** (1995) 501; M. Persic, P. Salucci, and F. Stel, *MNRAS* **281** (1996) 27P.
2. D. N. Spergel *et al.* [WMAP Collaboration], *Astrophys. J. Suppl.* **170** (2007) 377 [arXiv:astro-ph/0603449].
3. A. G. Riess *et al.*, *A. J.* **116** (1998) 1009; P. Garnovich *et al.* *Ap. J.* **509** (1998) 74; S. Perlmutter *et al.*, *Ap. J.* **517** (1999) 565; J.L. Tonry *et al.* *Ap. J.* **594** (2003) 1; R.A. Knop *et al.* *Ap. J.* **598** (2003) 102; A. G. Riess *et al.* *Ap. J.* **607** (2004) 665.
4. D. J. Eisenstein *et al.* [SDSS Collaboration], *Astrophys. J.* **633** (2005) 560 [arXiv:astro-ph/0501171].
5. D. Wittman, *et al.*, *Astrophys. J.* **643**, 128 (2006) [arXiv:astro-ph/0507606].
6. D. Clowe, *et al.*, *Astrophys. J.* **648** (2006) L109 [arXiv:astro-ph/0608407].
7. K. A. Olive, arXiv:astro-ph/0301505.
8. P. Fayet, *Phys. Lett.* **B64** (1976) 159; *Phys. Lett.* **B69** (1977) 489; *Phys. Lett.* **B84** (1979) 416.
9. H.E. Haber and G.L. Kane, *Phys.Rep.* **117** (1985) 75.
10. L. Girardello and M.T. Grisaru *Nucl. Phys.* **B194** (1982) 65.
11. S. P. Martin, arXiv:hep-ph/9709356; J. R. Ellis, arXiv:hep-ph/9812235; K. A. Olive, arXiv:hep-ph/9911307; M. E. Peskin, arXiv:0801.1928 [hep-ph].
12. J. Ellis, J.S. Hagelin, D.V. Nanopoulos, K.A. Olive and M. Srednicki, *Nucl. Phys. B* **238** (1984) 453; see also H. Goldberg, *Phys. Rev. Lett.* **50** (1983) 1419.
13. R. Watkins, M. Srednicki and K. A. Olive, *Nucl. Phys.* **B310** (1988) 693.

14. P. Hut, *Phys. Lett.* **B69** (1977) 85; B. W. Lee and S. Weinberg, *Phys. Rev. Lett.* **39** (1977) 165; M. I. Vysotsky, A. D. Dolgov and Y. B. Zeldovich, *Pisma Zh. Eksp. Teor. Fiz.* **26** (1977) 200.
15. G. Steigman, K. A. Olive, and D. N. Schramm, *Phys. Rev. Lett.* **43** (1979) 239; K. A. Olive, D. N. Schramm, and G. Steigman, *Nucl. Phys.* **B180** (1981) 497.
16. K. Griest and D. Seckel, *Phys. Rev.* **D43** (1991) 3191.
17. J. R. Ellis, S. Kelley and D. V. Nanopoulos, *Phys. Lett. B* **260** (1991) 131; U. Amaldi, W. de Boer and H. Furstenuau, *Phys. Lett. B* **260** (1991) 447; P. Langacker and M. x. Luo, *Phys. Rev. D* **44** (1991) 817; C. Giunti, C. W. Kim and U. W. Lee, *Mod. Phys. Lett. A* **6** (1991) 1745.
18. For reviews, see: H. P. Nilles, *Phys. Rep.* **110** (1984) 1; A. Brignole, L. E. Ibanez and C. Munoz, arXiv:hep-ph/9707209, published in *Perspectives on supersymmetry*, ed. G. L. Kane, pp. 125-148.
19. M. Drees and M. M. Nojiri, *Phys. Rev. D* **47** (1993) 376 [arXiv:hep-ph/9207234]; H. Baer and M. Brhlik, *Phys. Rev. D* **53** (1996) 597 [arXiv:hep-ph/9508321]; *Phys. Rev. D* **57** (1998) 567 [arXiv:hep-ph/9706509]; H. Baer, M. Brhlik, M. A. Diaz, J. Ferrandis, P. Mercadante, P. Quintana and X. Tata, *Phys. Rev. D* **63** (2001) 015007 [arXiv:hep-ph/0005027]; A. B. Lahanas, D. V. Nanopoulos and V. C. Spanos, *Mod. Phys. Lett. A* **16** (2001) 1229 [arXiv:hep-ph/0009065].
20. J. R. Ellis, T. Falk, K. A. Olive and M. Schmitt, *Phys. Lett. B* **388** (1996) 97 [arXiv:hep-ph/9607292]; *Phys. Lett. B* **413** (1997) 355 [arXiv:hep-ph/9705444]; J. R. Ellis, T. Falk, G. Ganis, K. A. Olive and M. Schmitt, *Phys. Rev. D* **58** (1998) 095002 [arXiv:hep-ph/9801445]; V. D. Barger and C. Kao, *Phys. Rev. D* **57** (1998) 3131 [arXiv:hep-ph/9704403]; J. R. Ellis, T. Falk, G. Ganis and K. A. Olive, *Phys. Rev. D* **62** (2000) 075010 [arXiv:hep-ph/0004169]; V. D. Barger and C. Kao, *Phys. Lett. B* **518** (2001) 117 [arXiv:hep-ph/0106189]; L. Roszkowski, R. Ruiz de Austri and T. Nihei, *JHEP* **0108** (2001) 024 [arXiv:hep-ph/0106334]; A. B. Lahanas and V. C. Spanos, *Eur. Phys. J. C* **23** (2002) 185 [arXiv:hep-ph/0106345]; A. Djouadi, M. Drees and J. L. Kneur, *JHEP* **0108** (2001) 055 [arXiv:hep-ph/0107316]; U. Chattopadhyay, A. Corsetti and P. Nath, *Phys. Rev. D* **66** (2002) 035003 [arXiv:hep-ph/0201001]; J. R. Ellis, K. A. Olive and Y. Santoso, *New Jour. Phys.* **4** (2002) 32 [arXiv:hep-ph/0202110]; H. Baer, C. Balazs, A. Belyaev, J. K. Mizukoshi, X. Tata and Y. Wang, *JHEP* **0207** (2002) 050 [arXiv:hep-ph/0205325]; R. Arnowitt and B. Dutta, arXiv:hep-ph/0211417.
21. J. R. Ellis, T. Falk, G. Ganis, K. A. Olive and M. Srednicki, *Phys. Lett. B* **510** (2001) 236 [arXiv:hep-ph/0102098].
22. J. R. Ellis, K. A. Olive, Y. Santoso and V. C. Spanos, *Phys. Lett. B* **565** (2003) 176 [arXiv:hep-ph/0303043].
23. H. Baer and C. Balazs, *JCAP* **0305**, 006 (2003) [arXiv:hep-ph/0303114]; A. B. Lahanas and D. V. Nanopoulos, *Phys. Lett. B* **568**, 55 (2003) [arXiv:hep-ph/0303130]; U. Chattopadhyay, A. Corsetti and P. Nath, *Phys. Rev. D* **68**, 035005 (2003) [arXiv:hep-ph/0303201]; . Munoz, *Int. J. Mod. Phys. A* **19**, 3093 (2004) [arXiv:hep-ph/0309346].
24. L.E. Ibáñez and G.G. Ross, *Phys. Lett.* **B110** (1982) 215; L.E. Ibáñez, *Phys. Lett.* **B118** (1982) 73; J. Ellis, D.V. Nanopoulos and K. Tamvakis, *Phys. Lett.* **B121** (1983) 123; J. Ellis, J. Hagelin, D.V. Nanopoulos and K. Tamvakis, *Phys. Lett.* **B125** (1983) 275; L. Alvarez-Gaumé, J. Polchinski, and M. Wise, *Nucl. Phys.* **B221** (1983) 495.
25. R. Barbieri, S. Ferrara and C.A. Savoy, *Phys. Lett.* **119B** (1982) 343.
26. J. R. Ellis, K. A. Olive, Y. Santoso and V. C. Spanos, *Phys. Lett. B* **573** (2003) 162 [arXiv:hep-ph/0305212]; J. R. Ellis, K. A. Olive, Y. Santoso and V. C. Spanos, *Phys. Rev. D* **70** (2004) 055005 [arXiv:hep-ph/0405110].
27. J. Polonyi, Budapest preprint KFKI-1977-93 (1977);
28. J. R. Ellis, K. A. Olive and P. Sandick, *Phys. Lett. B* **642** (2006) 389 [arXiv:hep-ph/0607002]; *JHEP* **0706** (2007) 079 [arXiv:0704.3446 [hep-ph]].
29. D. Matalliotakis and H. P. Nilles, *Nucl. Phys. B* **435** (1995) 115 [arXiv:hep-ph/9407251]; M. Olechowski and S. Pokorski, *Phys. Lett. B* **344**, 201 (1995) [arXiv:hep-ph/9407404]; V. Berezhinsky, A. Bottino, J. Ellis, N. Fornengo, G. Mignola and S. Scopel, *Astropart. Phys.* **5** (1996) 1, hep-ph/9508249; M. Drees, M. Nojiri, D. Roy and Y. Yamada, *Phys. Rev. D* **56** (1997) 276, [Erratum-ibid. **D 64** (1997) 039901], hep-ph/9701219; M. Drees, Y. Kim, M. Nojiri, D. Toya, K. Hasuko and T. Kobayashi, *Phys. Rev. D* **63** (2001) 035008, hep-ph/0007202; P. Nath and R. Arnowitt, *Phys. Rev. D* **56** (1997) 2820, hep-ph/9701301; J. R. Ellis, T. Falk, G. Ganis, K. A. Olive and M. Schmitt, *Phys. Rev. D* **58** (1998) 095002 [arXiv:hep-ph/9801445]; J. R. Ellis, T. Falk, G. Ganis and K. A. Olive, *Phys. Rev. D* **62** (2000) 075010 [arXiv:hep-ph/0004169]; A. Bottino, F. Donato, N. Fornengo and S. Scopel, *Phys. Rev. D* **63** (2001) 125003, hep-ph/0010203; S. Profumo, *Phys. Rev. D* **68** (2003) 015006, hep-ph/0304071; D. Cerdeno and C. Munoz, *JHEP* **0410** (2004) 015, hep-ph/0405057; H. Baer, A. Mustafayev, S. Profumo, A. Belyaev and X. Tata, *JHEP* **0507** (2005) 065, hep-ph/0504001.
30. J. Ellis, K. Olive and Y. Santoso, *Phys. Lett. B* **539**, 107 (2002) [arXiv:hep-ph/0204192]; J. R. Ellis, T. Falk, K. A. Olive and Y. Santoso, *Nucl. Phys. B* **652**, 259 (2003) [arXiv:hep-ph/0210205].
31. J. Ellis, T. Falk, and K.A. Olive, *Phys. Lett.* **B444** (1998) 367 [arXiv:hep-ph/9810360]; J. Ellis, T. Falk, K.A. Olive, and M. Srednicki, *Astr. Part. Phys.* **13** (2000) 181 [Erratum-ibid. **15** (2001) 413] [arXiv:hep-ph/9905481].
32. Joint LEP 2 Supersymmetry Working Group, *Combined LEP Chargino Results, up to 208 GeV*, http://lepsusy.web.cern.ch/lepsusy/www/inos-moriond01/charginos_pub.html.
33. Joint LEP 2 Supersymmetry Working Group, *Combined LEP Selectron/Smuon/Stau Results, 183-208 GeV*, http://lepsusy.web.cern.ch/lepsusy/www/sleptons-summer02/slep_2002.html.
34. LEP Higgs Working Group for Higgs boson searches, OPAL Collaboration, ALEPH Collaboration, DELPHI Collaboration and L3 Collaboration, *Phys. Lett. B* **565** (2003) 61 [arXiv:hep-ex/0306033]. *Search for neutral Higgs bosons at LEP*, paper submitted to ICHEP04, Beijing, LHWG-NOTE-2004-01, ALEPH-2004-008, DELPHI-2004-042, L3-NOTE-2820, OPAL-TN-744, <http://lep Higgs.web.cern.ch/LEPHIGGS/papers/August2004.MSSM/index.html>.
35. S. Heinemeyer, W. Hollik and G. Weiglein, *Comput. Phys. Commun.* **124** (2000) 76 [arXiv:hep-ph/9812320]; S. Heinemeyer, W. Hollik and G. Weiglein, *Eur. Phys. J. C* **9** (1999) 343 [arXiv:hep-ph/9812472].

36. S. Chen *et al.* [CLEO Collaboration], *Phys. Rev. Lett.* **87** (2001) 251807 [arXiv:hep-ex/0108032]; P. Koppenburg *et al.* [Belle Collaboration], *Phys. Rev. Lett.* **93** (2004) 061803 [arXiv:hep-ex/0403004]. B. Aubert *et al.* [BaBar Collaboration], arXiv:hep-ex/0207076; E. Barberio *et al.* [Heavy Flavor Averaging Group (HFAG)], arXiv:hep-ex/0603003.
37. C. Degrossi, P. Gambino and G. F. Giudice, *JHEP* **0012** (2000) 009 [arXiv:hep-ph/0009337], as implemented by P. Gambino and G. Ganis.
38. [The Muon $g-2$ Collaboration], *Phys. Rev. Lett.* **92** (2004) 161802, hep-ex/0401008; G. Bennett *et al.* [The Muon $g-2$ Collaboration], *Phys. Rev. D* **73** (2006) 072003 [arXiv:hep-ex/0602035].
39. M. Davier, S. Eidelman, A. Höcker and Z. Zhang, *Eur. Phys. J. C* **31** (2003) 503, hep-ph/0308213; see also M. Knecht, *Lect. Notes Phys.* **629**, 37 (2004) [arXiv:hep-ph/0307239]; K. Melnikov and A. Vainshtein, *Phys. Rev. D* **70** (2004) 113006 [arXiv:hep-ph/0312226]; J. F. de Troconiz and F. J. Yndurain, *Phys. Rev. D* **71**, 073008 (2005) [arXiv:hep-ph/0402285]; M. Passera, arXiv:hep-ph/0411168; K. Hagiwara, A. Martin, D. Nomura and T. Teubner, *Phys. Lett. B* **649** (2007) 173 [arXiv:hep-ph/0611102]; M. Davier, *Nucl. Phys. Proc. Suppl.* **169**, 288 (2007) [arXiv:hep-ph/0701163]; F. Jegerlehner, *Acta Phys. Polon. B* **38**, 3021 (2007) [arXiv:hep-ph/0703125]; J. Miller, E. de Rafael and B. Roberts, *Rept. Prog. Phys.* **70** (2007) 795 [arXiv:hep-ph/0703049]; S. Eidelman, talk given at the ICHEP06, Moscow, July 2006, see: http://ichep06.jinr.ru/reports/333_6s1_9p30_Eidelman.pdf.
40. J. L. Feng, K. T. Matchev and T. Moroi, *Phys. Rev. D* **61** (2000) 075005 [arXiv:hep-ph/9909334].
41. A. Romanino and A. Strumia, *Phys. Lett. B* **487** (2000) 165 [arXiv:hep-ph/9912301]. J. Ellis and K. Olive, *Phys. Lett. B* **514** (2001) 114, hep-ph/0105004.
42. J. R. Ellis, A. Ferstl and K. A. Olive, *Phys. Lett. B* **481**, 304 (2000) [arXiv:hep-ph/0001005]; J. R. Ellis, A. Ferstl and K. A. Olive, *Phys. Rev. D* **63**, 065016 (2001) [arXiv:hep-ph/0007113]; J. R. Ellis, A. Ferstl and K. A. Olive, *Phys. Lett. B* **532**, 318 (2002) [arXiv:hep-ph/0111064].
43. M. A. Shifman, A. I. Vainshtein and V. I. Zakharov, *Phys. Lett.* **78B**, 443 (1978); A. I. Vainshtein, V. I. Zakharov and M. A. Shifman, *Usp. Fiz. Nauk* **130**, 537 (1980).
44. J. Gasser, H. Leutwyler, and M. E. Sainio, *Phys. Lett. B* **253**, 252 (1991); M. Knecht, hep-ph/9912443 M. E. Sainio, *PiN Newsl.* **16**, 138 (2002) [arXiv:hep-ph/0110413].
45. W. M. Yao *et al.* [Particle Data Group], *J. Phys. G* **33** (2006) 1 and 2007 partial update for the 2008 edition available on the PDG WWW pages (URL: <http://pdg.lbl.gov/>).
46. Y. Goto *et al.* [Asymmetry Analysis collaboration], *Phys. Rev. D* **62**, 034017 (2000) [arXiv:hep-ph/0001046].
47. E. Leader, A. V. Sidorov and D. B. Stamenov, *Phys. Rev. D* **67**, 074017 (2003) [arXiv:hep-ph/0212085].
48. M. Alekseev *et al.* [COMPASS Collaboration], *Phys. Lett. B* **660**, 458 (2008) [arXiv:0707.4077 [hep-ex]].
49. J. Ellis, K. A. Olive and C. Savage, *Phys. Rev. D* **77**, 065026 (2008) [arXiv:0801.3656 [hep-ph]].
50. J. Binney and S. Tremaine, *Galactic Dynamics*, Princeton University Press, Princeton, p. 226 (1987).
51. G. Jungman, M. Kamionkowski and K. Griest, *Phys. Rept.* **267**, 195 (1996) [arXiv:hep-ph/9506380].
52. E. I. Gates, G. Gyuk and M. S. Turner, *Astrophys. J.* **449**, L123 (1995) [arXiv:astro-ph/9505039].
53. M. Kamionkowski and A. Kinkhabwala, *Phys. Rev. D* **57**, 3256 (1998) [arXiv:hep-ph/9710337].
54. M. Kamionkowski and S. M. Koushiappas, arXiv:0801.3269 [astro-ph].
55. K. A. Olive, arXiv:0709.3303 [hep-ph].
56. D. S. Akerib *et al.* [CDMS Collaboration], *Phys. Rev. Lett.* **96**, 011302 (2006) [arXiv:astro-ph/0509259].
57. J. Angle *et al.* [XENON Collaboration], *Phys. Rev. Lett.* **100**, 021303 (2008) [arXiv:0706.0039 [astro-ph]].
58. J. R. Ellis, K. A. Olive, Y. Santoso and V. C. Spanos, *Phys. Rev. D* **71**, 095007 (2005) [arXiv:hep-ph/0502001].
59. M. Battaglia *et al.*, *Eur. Phys. J. C* **22**, 535 (2001) [arXiv:hep-ph/0106204]; M. Battaglia, A. De Roeck, J. R. Ellis, F. Gianotti, K. A. Olive and L. Pape, *Eur. Phys. J. C* **33**, 273 (2004) [arXiv:hep-ph/0306219]; A. De Roeck, J. R. Ellis, F. Gianotti, F. Moortgat, K. A. Olive and L. Pape, *Eur. Phys. J. C* **49**, 1041 (2007) [arXiv:hep-ph/0508198].
60. Z. Ahmed *et al.* [CDMS Collaboration], arXiv:0802.3530 [astro-ph].
61. J. Ellis, S. Heinemeyer, K. Olive and G. Weiglein, *JHEP* **0502** 013 (2005) [arXiv:hep-ph/0411216].
62. J. R. Ellis, S. Heinemeyer, K. A. Olive and G. Weiglein, *JHEP* **0605**, 005 (2006) [arXiv:hep-ph/0602220].
63. J. Ellis, S. Heinemeyer, K. Olive, A.M. Weber and G. Weiglein, *JHEP* **0708** (2007) 083 [arXiv:0706.0652 [hep-ph]].
64. K. Choi, K. S. Jeong and K. i. Okumura, *JHEP* **0509** (2005) 039 [arXiv:hep-ph/0504037]; M. Endo, M. Yamaguchi and K. Yoshioka, *Phys. Rev. D* **72** (2005) 015004 [arXiv:hep-ph/0504036]; A. Falkowski, O. Lebedev and Y. Mambrini, *JHEP* **0511** (2005) 034 [arXiv:hep-ph/0507110]; R. Kitano and Y. Nomura, *Phys. Lett. B* **631** (2005) 58 [arXiv:hep-ph/0509039]; R. Kitano and Y. Nomura, *Phys. Rev. D* **73** (2006) 095004 [arXiv:hep-ph/0602096]; A. Pierce and J. Thaler, *JHEP* **0609** (2006) 017 [arXiv:hep-ph/0604192]; K. Kawagoe and M. M. Nojiri, *Phys. Rev. D* **74**, 115011 (2006) [arXiv:hep-ph/0606104]; H. Baer, E.-K. Park, X. Tata and T. T. Wang, *JHEP* **0608** (2006) 041 [arXiv:hep-ph/0604253]; K. Choi, K. Y. Lee, Y. Shimizu, Y. G. Kim and K. i. Okumura, *JCAP* **0612** (2006) 017 [arXiv:hep-ph/0609132]; O. Lebedev, V. Lowen, Y. Mambrini, H. P. Nilles and M. Ratz, *JHEP* **0702** (2007) 063 [arXiv:hep-ph/0612035].
65. H. Itoh, N. Okada and T. Yamashita, *Phys. Rev. D* **74**, 055005 (2006) [arXiv:hep-ph/0606156].
66. S. Kachru, R. Kallosh, A. Linde and S. P. Trivedi, *Phys. Rev. D* **68** (2003) 046005 [arXiv:hep-th/0301240]; K. Choi, A. Falkowski, H. P. Nilles and M. Olechowski, *Nucl. Phys. B* **718** (2005) 113 [arXiv:hep-th/0503216].
67. D. Tovey, *Eur. Phys. J. direct C* **4** CN4 (2002).
68. The CMS Collaboration, *CMS Physics Technical Design Report. Volume II: Physics Performance*, CERN/LHCC 2006-021, CMS TDR 8.2 (2006), see: <http://cmsdoc.cern.ch/cms/cpt/tdr/>.
69. D. Tovey, private communication to P. Sandick.
70. J. Ellis, K. A. Olive and P. Sandick, arXiv:0801.1651 [hep-ph].
71. J. R. Ellis, K. A. Olive, Y. Santoso and V. C. Spanos, *Phys. Lett. B* **588** (2004) 7 [arXiv:hep-ph/0312262]; J. L. Feng, A. Rajaraman and F. Takayama, *Phys. Rev. Lett.* **91**

- (2003) 011302 [arXiv:hep-ph/0302215]; J. L. Feng, S. Su and F. Takayama, *Phys. Rev. D* **70** (2004) 075019 [arXiv:hep-ph/0404231].
72. R. H. Cyburt, J. R. Ellis, B. D. Fields and K. A. Olive, *Phys. Rev. D* **67** (2003) 103521 [arXiv:astro-ph/0211258]; J. L. Feng, S. f. Su and F. Takayama, *Phys. Rev. D* **70** (2004) 063514 [arXiv:hep-ph/0404198]; J. R. Ellis, K. A. Olive and E. Vangioni, *Phys. Lett. B* **619**, 30 (2005) [arXiv:astro-ph/0503023]; K. Kohri, T. Moroi and A. Yotsuyanagi, *Phys. Rev. D* **73** (2006) 123511 [arXiv:hep-ph/0507245]; D. G. Cerdeno, K. Y. Choi, K. Jedamzik, L. Roszkowski and R. Ruiz de Austri, *JCAP* **0606** (2006) 005 [arXiv:hep-ph/0509275]; F. D. Steffen, *JCAP* **0609**, 001 (2006) [arXiv:hep-ph/0605306].
73. M. Pospelov, *Phys. Rev. Lett.* **98** (2007) 231301 [arXiv:hep-ph/0605215]; K. Hamaguchi, T. Hatsuda, M. Kamimura, Y. Kino and T. T. Yanagida, *Phys. Lett. B* **650** (2007) 268 [arXiv:hep-ph/0702274]; C. Bird, K. Koopmans and M. Pospelov, arXiv:hep-ph/0703096.
74. R. H. Cyburt, J. R. Ellis, B. D. Fields, K. A. Olive and V. C. Spanos, *JCAP* **0611** (2006) 014 [arXiv:astro-ph/0608562].
75. K. Jedamzik, *Phys. Rev. D* **70** (2004) 063524 [arXiv:astro-ph/0402344]; K. Jedamzik, *Phys. Rev. D* **70** (2004) 083510 [arXiv:astro-ph/0405583].
76. G. Sigl, K. Jedamzik, D. N. Schramm and V. S. Berezinsky, *Phys. Rev. D* **52** (1995) 6682 [arXiv:astro-ph/9503094].
77. J. R. Ellis, K. A. Olive and V. C. Spanos, *Phys. Lett. B* **624** (2005) 47 [arXiv:hep-ph/0504196]; J. R. Ellis, K. A. Olive, Y. Santoso and V. C. Spanos, *JHEP* **0605**, 063 (2006) [arXiv:hep-ph/0603136].
78. J. Ellis, T. Hahn, S. Heinemeyer, K. A. Olive and G. Weiglein, *JHEP* **0710**, 092 (2007) [arXiv:0709.0098 [hep-ph]].
79. S. Gennai, A. Nikitenko and L. Wendland, CMS Note 2006/126.
80. R. Kinnunen and S. Lehti, CMS Note 2006/075.
81. A. Kalinowski, M. Konecki and D. Kotlinski, CMS Note 2006/105.
82. S. Gennai, S. Heinemeyer, A. Kalinowski, R. Kinnunen, S. Lehti, A. Nikitenko and G. Weiglein, *Eur. Phys. J. C* **52**, 383 (2007) [arXiv:0704.0619 [hep-ph]].
83. A. Abulencia et al. [CDF Collaboration], *Phys. Rev. Lett.* **96** (2006) 011802, hep-ex/0508051.
84. V. Abazov et al. [D0 Collaboration], *Phys. Rev. Lett.* **97** (2006) 121802, hep-ex/0605009.
85. A. Abulencia et al. [CDF Collaboration], *Phys. Rev. Lett.* **96** (2006) 042003, hep-ex/0510065.
86. CDF Collaboration, CDF note 8676, see:
http://www-cdf.fnal.gov/~aa/mssm_htt_1fb/note/cdf8676.pdf.
87. D0 Collaboration, D0 Note 5331-CONF, see:
<http://www-d0.fnal.gov/cgi-bin/d0note?5331>.
88. M. Carena, S. Heinemeyer, C. Wagner and G. Weiglein, *Eur. Phys. J. C* **45** (2006) 797, hep-ph/0511023.
89. A. Djouadi and Y. Mambrini, *JHEP* **0612** (2006) 001, hep-ph/0609234.
90. J. R. Ellis, S. Heinemeyer, K. A. Olive and G. Weiglein, *Phys. Lett. B* **653**, 292 (2007) [arXiv:0706.0977 [hep-ph]].
91. D. Acosta et al. [CDF Collaboration], *Phys. Rev. Lett.* **93** (2004) 032001 [arXiv:hep-ex/0403032]; V. M. Abazov et al. [D0 Collaboration], *Phys. Rev. Lett.* **94**, 071802 (2005) [arXiv:hep-ex/0410039]; The D0 Collaboration, D0note, 4733-CONF;
- <http://www-d0.fnal.gov/Run2Physics/WWW/results/prelim/B/B21/B21.pdf>; M. Herndon, The CDF and D0 Collaborations, FERMILAB-CONF-04-391-E. Published Proceedings 32nd International Conference on High-Energy Physics (ICHEP 04), Beijing, China, August 16-22, 2004; The CDF Collaboration, CDF note 7670; <http://www-cdf.fnal.gov/physics/new/bottom/050407.blessed-bsmumu/>.

